

# Deep Compositional Spatial Models

Andrew Zammit-Mangion

School of Math. and Applied Stat., University of Wollongong, Australia

Tin Lok James Ng

School of Math. and Applied Stat., University of Wollongong, Australia

Quan Vu

School of Math. and Applied Stat., University of Wollongong, Australia

Maurizio Filippone

Department of Data Science, EURECOM, France

## Abstract

Nonstationary, anisotropic spatial processes are often used when modelling, analysing and predicting complex environmental phenomena. One such class of processes considers a stationary, isotropic process on a warped spatial domain. The warping function is generally difficult to fit and not constrained to be bijective, often resulting in ‘space-folding.’ Here, we propose modelling a bijective warping function through a composition of multiple elemental bijective functions in a deep-learning framework. We consider two cases; first, when these functions are known up to some weights that need to be estimated, and, second, when the weights in each layer are random. Inspired by recent methodological and technological advances in deep learning and deep Gaussian processes, we employ approximate Bayesian methods to make inference with these models using graphical processing units. Through simulation studies in one and two dimensions we show that the deep compositional spatial models are quick to fit, and are able to provide better predictions and uncertainty quantification than other deep stochastic models of similar complexity. We also show their remarkable capacity to model highly nonstationary, anisotropic spatial data using radiances from the MODIS instrument aboard the Aqua satellite.

*Keywords:* Deep Models; Nonstationarity; Spatial Statistics; Stochastic Processes; Variational Bayes.

# 1 Introduction

Modelling non-stationarity in spatial processes is pivotal to obtaining reliable predictions and uncertainty quantification when analysing complex environmental phenomena. Several modelling classes have been constructed to model non-stationarity, ranging from convolution models to stochastic partial differential equation models, to mention a few (e.g., Higdon et al., 1999; Paciorek and Schervish, 2006; Fuglstad et al., 2015). Among the most well-known of these is the ‘warping approach’ of Sampson and Guttorp (1992). Consider a spatial process  $Y(\cdot)$  on some spatial domain  $G$ . Sampson and Guttorp proposed warping  $G$  under a mapping  $\mathbf{f} \equiv \mathbf{f}_1 : G \rightarrow D_1$  such that the process is stationary and isotropic on  $D_1$ . Their approach involves finding a multivariate function  $\mathbf{f}_1$  such that the covariance function of  $Y(\cdot)$  on the warped space,  $C_{D_1}(\mathbf{f}_1(\cdot), \mathbf{f}_1(\cdot))$ , is a univariate, positive-definite, function of distance, say  $C_{D_1}^o(h)$ , where  $h = \|\mathbf{u}_i - \mathbf{u}_j\|$ ,  $\mathbf{u}_i, \mathbf{u}_j \in D_1$ . In their case,  $\mathbf{f}_1$  was determined using multi-dimensional scaling (MDS) and thin-plate splines.

Sampson and Guttorp’s approach paved the path for a suite of spatial modelling tools largely motivated by the intuitive result of Perrin and Meiring (1999) who show that if  $\mathbf{f}_1$  is bijective, and if both it and its inverse are differentiable (specifically, if  $\mathbf{f}_1$  is a diffeomorphism), that then (under mild conditions) there is a one-to-one mapping between  $\{C_{D_1}^o(\cdot), \mathbf{f}_1\}$  and the nonstationary covariance function on  $G$ . In this case  $C_G(\cdot, \cdot)$  is said to be stationary isotropic reducible (Perrin and Senoussi, 2000). Sampson et al. (2001) provide a detailed review of deformation methods up to the year 2001, and discuss two methods that are of particular relevance to this work. The first of these is the approach of Smith (1996), in which the map  $\mathbf{f}_1$  is modelled using a sum of radial basis functions derived from the thin-plate spline, and a likelihood-based approach is used for estimating the deformation. The second is that of Perrin and Monestiez (1999) who used compositions of bijective radial basis function mappings to model  $\mathbf{f}_1$ . Bivariate Gaussian processes were first used to model the deformation map in a Bayesian setting by Schmidt and O’Hagan (2003), while Gaussian process deformations were also used in a state space framework by Morales et al. (2013).

An interesting connection can be made between these warping models and feedforward neural nets, which have garnered much interest in the past decade (e.g., LeCun et al., 2015) and that express the latent function  $\mathbf{f}$  through the composition of  $n$  hidden functions  $\mathbf{f}_n \circ \mathbf{f}_{n-1} \circ \dots \circ \mathbf{f}_1$ . Indeed, the model of Smith (1996) has  $n = 1$  hidden layer, while that of Perrin and Monestiez (1999) has  $n > 1$  hidden layers. The model developed by Schmidt and O’Hagan (2003) is a Gaussian process with one hidden layer, a special case of the general deep Gaussian process devised by Damianou and Lawrence (2013) and later extended by several authors including Hensman and Lawrence (2014) and Salimbeni and Deisenroth (2017).

This connection begs the question as to whether spatial models can be made more representational of the data-generation process when using a warping function  $\mathbf{f}$  which has  $n$  hidden layers, where  $n > 1$ . This connection is all the more interesting given the recent interest in understanding the expressive power of deep neural networks (Bengio and Delalleau, 2011; Eldan and Shamir, 2016; Safran and Shamir, 2017). In particular, it has been shown that deep networks are exponentially more efficient in function approximation

than shallow networks (Liang and Srikant, 2017; Arora et al., 2018). In Section 2 we review several models from both the statistical and machine-learning literature which can be used for deformation within a unifying modelling framework.

Bijectionality of  $\mathbf{f}$  has been an ongoing cause for concern for spatial statisticians: Sampson and Guttorp (1992) state that “a mapping that folds usually results in a model that overfits the sample,” while Schmidt and O’Hagan (2003) assert that it is “undesirable and/or implausible for environmental data.” Due to the nature of the problems generally considered in their domain, for the machine-learning community the lack of bijectionality is largely considered a non-issue (insofar as too much warping can lead to map degeneracy; see Duvenaud et al., 2014; Dunlop et al., 2018). On the other hand, various approaches have been used by spatial statisticians to enforce bijectionality, involving both soft (e.g., Meiring et al., 1997; Fouedjio et al., 2015) and hard (e.g., Iovleff and Perrin, 2004) constraints. While the latter generally lead to difficult optimisation problems, the former do not provide the bijectionality guarantees we seek, and the cautious modeller will fit deformations that are generally too smooth. These difficulties have rendered other methods that model non-stationarity directly through the covariance function in a way that validity is guaranteed (e.g., Paciorek and Schervish, 2006; Fuglstad et al., 2015), more attractive. Indeed, such models can capture stronger non-stationarity than what is possible using simple mappings that are known to be globally bijective, such as the Möbius transformation that we consider in Section 3. However, in this work we show that compositions of multiple maps can yield the desired flexibility we seek; further, at the cost of relatively few parameters.

The main novel contribution of our work is the construction of a flexible *deep compositional spatial model* in Section 3, which is built on the premise that a map constructed by composition of multiple bijective maps is itself bijective. We do not present the first instance of such a model: Perrin and Monestiez (1999) were probably the first to use multiple compositions of bijective radial basis function mappings to model  $\mathbf{f}$  in a spatial context. The flexible deep compositional spatial model we present extends their’s on various fronts. First, inspired by multi-resolutional spatial modelling tools (e.g., Nychka et al., 2015; Zammit-Mangion and Cressie, 2019), we use multi-resolutional warpings that capture deformations at various scales. Second, in addition to the functions in Perrin and Monestiez (1999) for the multiresolution basis, we also consider warping layers with axial warping (scaling) units as well as large-scale Möbius transformations (e.g., Dubrovin et al., 1992, Section 11.3) that are also diffeomorphisms. Finally, our model is seated in a likelihood framework and is designed to take full advantage of the computational tools designed for deep neural networks, such as stochastic gradient descent methods. This, in combination with the use of basis-function field representations for  $Y(\cdot)$  (Cressie and Johannesson, 2008), allows us to train relatively complex models in the presence of large data sets with relative ease.

In Section 4 we compare various approaches to doing spatial warping, including several types of deep Gaussian processes and our deep compositional spatial model, in a simulation experiment in one dimension. We also show the utility of our proposed model in two dimensions and on radiances using data from the MODIS instrument aboard the Aqua satellite. Section 5 concludes the work.

## 2 Deep Models for Spatial Data

In this section we review several deep models that have been used both in the statistical and the machine-learning literature and that are relevant to spatial deformation methods. We largely review them in a feedforward deep net framework, on which we also base the deep compositional spatial model in the next section. In order to facilitate the review, we have classified the models into two groups: input-warped Gaussian processes and deep stochastic processes. The primary distinction between these two groups is that while models in the former class treat the warping as deterministic (resulting in covariances that can be evaluated deterministically for any two spatial locations), the latter treats the warping as a random process in itself (resulting in covariances that are themselves random). There is, of course, much modelling overlap between the two classes. Throughout this section we only consider processes that are formed through function *composition*: As shown by Dunlop et al. (2018), there are other ways to construct deep processes (e.g., by extending the work of Paciorek and Schervish, 2006, to multiple layers) but we do not consider those models here. We also focus on warpings that are low-rank; we give a brief review of models with nonparametric warpings at the end of Sections 2.1 and 2.2.

### 2.1 Input-warped Gaussian processes

Let  $Y(\cdot)$  be a Gaussian process on  $G$  with covariance function  $C_G(\mathbf{s}, \mathbf{u})$ ,  $\mathbf{s}, \mathbf{u} \in G$ . Assume that we have access to  $N$  noisy observations of  $Y(\cdot)$ , that is,

$$Z(\mathbf{s}_i) = Y(\mathbf{s}_i) + \epsilon_i, \quad i = 1, \dots, N, \quad (1)$$

where  $\epsilon_i \sim \text{Gau}(0, \sigma_\epsilon^2)$ ,  $\sigma_\epsilon^2$  is the measurement-error variance, and  $\mathbf{s}_1, \dots, \mathbf{s}_N \in G$  are the measurement locations. Then, inference on  $Y(\mathbf{s})$ ,  $\mathbf{s} \in G$ , is straightforward through Gaussian process regression if  $C_G(\cdot, \cdot)$  is known (e.g., Rasmussen and Williams, 2006, Chapter 2). Input-warped Gaussian processes (IWGPs) are built on the premise that although  $C_G(\cdot, \cdot)$  is very complicated, there exists a function  $C_{D_n}(\mathbf{f}(\cdot), \mathbf{f}(\cdot))$  that is simple, indeed simple enough to be expressed as a standard stationary, isotropic, covariance function  $C_{D_n}^o(\cdot)$ . The problem then reduces to finding  $\mathbf{f}(\cdot)$  and some parameters that define  $C_{D_n}^o(\cdot)$  (although occasionally  $C_{D_n}^o$  is also modelled nonparametrically).

In IWGP models,  $\mathbf{f}$  is a deterministic (yet unknown) mapping constructed through composition. Specifically,  $\mathbf{f} \equiv \mathbf{f}_n \circ \mathbf{f}_{n-1} \circ \dots \circ \mathbf{f}_1$  and

$$C_G(\mathbf{s}, \mathbf{u}) \equiv C_{D_n}^o(\|\mathbf{f}_n \circ \mathbf{f}_{n-1} \circ \dots \circ \mathbf{f}_1(\mathbf{s}) - \mathbf{f}_n \circ \mathbf{f}_{n-1} \circ \dots \circ \mathbf{f}_1(\mathbf{u})\|), \quad \mathbf{s}, \mathbf{u} \in G.$$

In the machine-learning literature,  $C_{D_n}^o(\cdot)$  is often referred to as a deep kernel (e.g., Wilson et al., 2016) and the resulting process as a manifold GP (Calandra et al., 2016).

#### 2.1.1 Low-rank IWGPs

As we shall see in this section, the IWGPs most commonly used are structured feedforward neural nets. That is, for some  $r_i$  basis functions at the  $i$ th layer,  $\phi_i(\cdot; \Theta_i) \equiv (\phi_{ij}(\cdot; \Theta_i) :$

$j = 1, \dots, r_i)'$ , and basis-function coefficients (or weights) at the  $i$ th layer  $\mathbf{W}_i(\Theta_i) \equiv (w_{ikj}(\Theta_i) : k = 1, \dots, d_i; j = 1, \dots, r_i)$  that map the input to a  $d_i$ -dimensional output,

$$\mathbf{f}_i(\mathbf{s}) = \mathbf{W}_i(\Theta_i)\phi_i(\mathbf{s}; \Theta_i), \quad \mathbf{s} \in D_{i-1}; \quad i = 1, \dots, n,$$

where  $\mathbf{f}_i : D_{i-1} \rightarrow D_i, i = 1, \dots, n, D_i \subset \mathbb{R}^{d_i}, D_0 \equiv G$ , and  $\Theta_i$  are parameters appearing inside the  $i$ th layer that can be either fixed or estimated. In most applications the weights  $\mathbf{W}_i$  are not parameterised in terms of the  $\Theta_i$  and these parameters only appear inside the basis functions, but as we show in Section 2.2.1 this is not always the case. The basis functions used and the constraints imposed on the weights  $\{\mathbf{W}_i\}$  generally dictate the type of IWGP.

The simplest  $n = 1$  low-rank IWGP is the single index linear model (Choi et al., 2011) where the input space is collapsed onto one dimension using a linear transformation. Specifically,  $\phi_1(\mathbf{s}) = \mathbf{s}$  and therefore  $f_1(\mathbf{s}) = (w_{111}, w_{112}, \dots)\mathbf{s}$ . Multiple index linear models collapse the input space into one of a smaller dimension that is greater than one, and thus  $\mathbf{f}_1(\mathbf{s}) = \mathbf{W}_1\mathbf{s}$ , where the number of rows in  $\mathbf{W}_1$  is less than the dimension of  $\mathbf{s}$ .

Marmin et al. (2018) augment the multiple index linear model by adding a second layer with  $\phi_2(\mathbf{s}; \Theta_2)$  set to Beta cumulative distribution functions (CDFs), which were also used for axial warping by Snoek et al. (2014). The (nonlinear) axial warping in the second layer results in a bijective map, but the first, dimension reduction, map is generally non-bijective: as a result, the index-models architectures are not bijective in general. Also, since spatial problems are low-dimensional problems, there is not much to be gained by using the encoding facility of index models.

Smith (1996) considered a spatial domain indexed by  $\mathbf{s} \in \mathbb{R}^2$ , set  $n = 1$ , and constructed  $\phi_1(\cdot)$  using basis functions that reconstruct thin-plate splines. Constraints were placed on  $\mathbf{W}_1$  to ensure identifiability. As with the original MDS/thin-plate spline approach of Sampson and Guttorp (1992), Smith’s mapping is not bijective in general and is structurally identical to traditional neural nets constructed using smooth basis-function activations, such as the tanh function or the sigmoid function. Both Matérn and a class of Bessel-function mixtures were considered for modelling  $C_{D_1}^o(\cdot)$ .

Perrin and Monestiez (1999) let  $n > 1$ , and constructed  $\mathbf{f}$  from the composition of radial-basis-function (RBF) deformations. The squared-exponential RBF at the  $i$ th layer takes the form

$$\mathbf{f}_i(\mathbf{s}) = \mathbf{s} + w_i(\mathbf{s} - \boldsymbol{\gamma}_i) \exp(-a_i\|\mathbf{s} - \boldsymbol{\gamma}_i\|^2); \quad \mathbf{s} \in D_{i-1} \subset \mathbb{R}^2, \quad (2)$$

where  $\boldsymbol{\gamma}_i = (\gamma_{i1}, \gamma_{i2})'$  is the RBF centroid,  $a_i$  is a scaling factor,  $w_i$  controls the intensity of domain expansion/shrinkage, and  $\Theta_i \equiv (\boldsymbol{\gamma}_i', a_i)'$  is the parameter vector of the radial basis functions at the  $i$ th layer. In Section 3.2 we show how this RBF can be re-expressed as a weighted sum of basis functions, where the weights are constrained to ensure bijectivity. A squared exponential covariance function was used to model  $C_{D_1}^o(\cdot)$ . Perrin and Monestiez (1999)’s work is the only one that we are aware of that uses parametric bijective warpings other than axial warpings in a spatial modelling application.

The above mentioned IWGPs contain several parameters that are generally estimated in a maximum likelihood setting. In Section 2.2 we describe relatively newer models where the

weights themselves are random, so that the warpings are stochastic processes in themselves. In this latter setting, approximations are generally needed to make inference on the latent warpings.

### 2.1.2 Nonparametric IWGPs

In Section 2.1.1 we focused on low-rank warping approaches, however there is also a sizeable portion of literature that focuses on nonparametric warping functions. Sampson and Guttorp (1992) set  $n = 1$ , modelled  $\mathbf{f}_1 \in \mathbb{R}^2$  nonparametrically using thin-plate splines, and constructed  $C_{D_1}^o(\cdot)$  using a class of Gaussian probability mixtures. This same shallow kernel was used by Monestiez et al. (1993), Meiring et al. (1997), Zidek et al. (2000), Damian et al. (2001), and more recently by Kleiber (2016) for simulating nonstationary fields. Bornn et al. (2012) also used thin-plate splines but additionally considered dimension expansion (i.e., they let  $d_1 > 2$ ) in a way that guarantees bijectivity. We briefly discuss dimension-expansion approaches in Section 5.

Iovleff and Perrin (2004) set  $n = 1$  and found  $\mathbf{f}_1 : \mathbb{R}^2 \rightarrow \mathbb{R}^2$  at the observation locations using a constrained optimisation algorithm that enforces bijectivity and let  $C_{D_1}^o(\cdot)$  be the power exponential. Anderes and Stein (2008) deduced  $\mathbf{f}_1 : \mathbb{R}^2 \rightarrow \mathbb{R}^2$  from local deformations estimated at a set of locations and then interpolated them over  $G$ . Gibbs (1998, Section 3.10.3) modelled  $\mathbf{f}_1 : \mathbb{R}^2 \rightarrow \mathbb{R}^2$  by taking a path integral between any fixed point  $\mathbf{s}_0$  and  $\mathbf{s}$  of an arbitrary positive function (which is estimated for each component of  $\mathbf{f}_1$ ). Xiong et al. (2007) simplifies Gibbs' approach by warping each axis separately; this ensures bijectivity but axial warpings have limited flexibility when used on their own.

## 2.2 Deep stochastic processes

A deep stochastic process (DSP) is a model in which each warping function is itself a stochastic process. By far the most common DSP is the deep Gaussian process (DGP) where the finite-dimensional distributions over the inputs to each layer are multivariate Gaussian. Note that DSPs are, in general, non-Gaussian processes over the inputs in  $G$  (i.e., even when the DSP is a DGP). Both the finite-dimensional (low-rank) and the full-rank process representations of DSPs are of particular relevance to spatial deformation methods.

### 2.2.1 Low-rank DSPs

We first consider the ubiquitous low-rank DGP. Let  $d_i$  be the output dimension of the  $i$ th layer. Then, if one equips each row in  $\mathbf{W}_i$  (i.e.,  $\mathbf{w}_i^{(k)}, k = 1, \dots, d_i$ ) with an independent multivariate Gaussian distribution with mean zero and covariance matrix  $\Sigma_i^{(kk)}$ , then  $f_{ik}(\mathbf{s})$  is a zero-mean Gaussian process with covariance function  $C_{D_{i-1}}(\mathbf{s}, \mathbf{u}) = \phi_i(\mathbf{s})' \Sigma_i^{(kk)} \phi_i(\mathbf{u})$ . More generally, if one equips  $\text{vec}(\mathbf{W}_i) \equiv (\mathbf{w}_i^{(k)'} : k = 1, \dots, d_i)'$  with a multivariate Gaussian distribution with mean zero, and valid block covariance matrix  $\Sigma_i \equiv (\Sigma_i^{(kk')} : k, k' = 1, \dots, d_i)$ , then  $\mathbf{f}_i$  is a multivariate Gaussian process with cross-covariance function matrix

$\mathbf{C}_{D_{i-1}}(\mathbf{s}, \mathbf{u}) = (\boldsymbol{\phi}_i(\mathbf{s})' \boldsymbol{\Sigma}_i^{(kk')} \boldsymbol{\phi}_i(\mathbf{u}) : k, k' = 1, \dots, d_i)$ . Instead of leaving  $\boldsymbol{\Sigma}_i$  general positive-definite, one often gives it the form  $\boldsymbol{\Sigma}_i \equiv \mathbf{R}_i \otimes \boldsymbol{\Sigma}_i^{(11)}$  where  $\otimes$  is the Kronecker product, and  $\mathbf{R}_i$  and  $\boldsymbol{\Sigma}_i^{(11)}$  are  $d_i \times d_i$  and  $r_i \times r_i$  positive-definite matrices, respectively. This modelling choice is usually made to reduce the number of parameters that need to be estimated and to take advantage of the computational benefits associated with the Kronecker product.

Cutajar et al. (2017) consider a straightforward parameteric DGP where  $\text{Var}(\mathbf{w}_i^{(k)}) = \mathbf{I}$ ,  $k = 1, \dots, d_i$ , and where  $\boldsymbol{\phi}_i(\cdot; \boldsymbol{\Theta}_i)$ ,  $i = 1, \dots, n$ , is a Fourier basis. Since the  $\boldsymbol{\Theta}_i$  are also treated as random, the basis functions are referred to as random Fourier features, previously used for Gaussian process modelling by Lázaro-Gredilla et al. (2010) and further investigated recently by Hensman et al. (2017).

The deep Gaussian process of Damianou and Lawrence (2013) is based on compositions of sparse Gaussian processes (sparse GPs). Sparse GPs are low-dimensional representations of GPs, and thus Damianou and Lawrence (2013)'s model, as well as all derivative works (e.g., Hensman and Lawrence, 2014; Dai et al., 2016; Bui et al., 2016) can be classed as low-rank DGPs. A type of sparse GP, known as the subset-of-regressors approximation (Quiñero-Candela and Rasmussen, 2005) or the predictive process (Banerjee et al., 2008), can be written as a weighted sum of basis functions. Specifically, let  $k = 1$  and let the 'parent' GP at the  $i$ th layer have covariance function  $C_{D_{i-1}}(\cdot, \cdot)$ . Further, consider a set of  $m_i$  inducing points  $\bar{\mathbf{S}}_{i-1} \equiv (\bar{\mathbf{s}}_{i-1,1}, \dots, \bar{\mathbf{s}}_{i-1,m_i})$ . Then,

$$f_{i1}(\mathbf{s}) = \mathbf{w}_i^{(1)}(\bar{\mathbf{S}}_{i-1}, \boldsymbol{\Theta}_i)' \boldsymbol{\phi}_i(\mathbf{s}; \bar{\mathbf{S}}_{i-1}, \boldsymbol{\Theta}_i),$$

where

$$\begin{aligned} \boldsymbol{\phi}_i(\mathbf{s}; \bar{\mathbf{S}}_{i-1}, \boldsymbol{\Theta}_i) &\equiv (C_{D_{i-1}}(\mathbf{s}, \bar{\mathbf{s}}_{i-1,1}), \dots, C_{D_{i-1}}(\mathbf{s}, \bar{\mathbf{s}}_{i-1,m_i}))', \\ \mathbf{w}_i^{(1)}(\bar{\mathbf{S}}_{i-1}; \boldsymbol{\Theta}_i) &\sim \text{Gau}(\mathbf{0}, C_{D_{i-1}}(\bar{\mathbf{S}}_{i-1}, \bar{\mathbf{S}}_{i-1})^{-1}), \end{aligned}$$

where  $C_{D_{i-1}}(\bar{\mathbf{S}}_{i-1}, \bar{\mathbf{S}}_{i-1}) \equiv (C_{D_{i-1}}(\bar{\mathbf{s}}_{i-1,k}, \bar{\mathbf{s}}_{i-1,l}) : k, l = 1, \dots, m_i)$ .

In DGPs based on sparse GPs, both the inducing-point locations  $\bar{\mathbf{S}}_{i-1}$  and the covariance-function parameters  $\boldsymbol{\Theta}_i$  generally need to be estimated. Our experience (using the variational Bayes approximate inference scheme of Damianou and Lawrence (2013)) is that DGPs constructed by nesting sparse GPs are difficult to fit, even in the low-dimensional settings we consider.

In DGPs, since the hidden functions are multivariate Gaussian processes, they are in general not bijective (in the sense that sample paths from the hidden functions will fold). Bijective maps require the hidden layers to be non-Gaussian processes, and thus the model we require is a general deep stochastic process (DSP) that is non-Gaussian. Non-Gaussian DSPs can be highly complex processes, and to the best of our knowledge they have yet to be exploited for regression or classification tasks. In this article we present a deep compositional spatial process that is a non-Gaussian DSP. Specifically, it has the same structure as a DGP, but lets the weights in the hidden layers  $\mathbf{W}_i(\cdot)$ ,  $i = 1, \dots, n$ , be trans-Gaussian in order to ensure that sample paths at each of the hidden layers are bijective; see Section 3.

### 2.2.2 Full-rank DSPs

In full-rank DGPs, each layer is defined to be a multivariate Gaussian process, that is,  $\mathbf{f}_i(\cdot) \sim MVGP(\boldsymbol{\mu}_i(\cdot), \mathbf{C}_{D_{i-1}}(\cdot, \cdot); \boldsymbol{\Theta}_i)$ ,  $1 \leq i \leq n$ , where  $MVGP(\boldsymbol{\mu}_i(\cdot), \mathbf{C}_{D_{i-1}}(\cdot, \cdot); \boldsymbol{\Theta}_i)$  is a multivariate Gaussian process with mean vector function  $\boldsymbol{\mu}_i(\cdot)$  and cross-covariance function matrix  $\mathbf{C}_{D_{i-1}}(\cdot, \cdot)$ . Similar to the low-rank DGP, it is common to let  $\mathbf{C}_{D_{i-1}}(\cdot, \cdot) \equiv \mathbf{R}_i \otimes C_{D_{i-1}}(\cdot, \cdot)$ ; such models are said to be *separable*. There are connections between full-rank DGPs and low-rank DGPs where the number of hidden layers in the latter tends to infinity (e.g., Neal, 1996).

Full-rank Gaussian processes are computationally burdensome to work with since estimation and inference algorithms with them will necessitate the decomposition of matrices of size  $N \times N$ . Yet, for moderately-sized problems, they are still computationally tractable, and were used in a spatial deformation context by Schmidt and O’Hagan (2003) and Schmidt et al. (2011). Since we envision deep compositional spatial models to be useful in large data settings, from now on we restrict our attention to low-rank IWGPs and DSPs.

## 3 Deep Compositional Spatial Models

In this section we introduce a class of flexible deep compositional spatial models where the geographic domain is warped through a composition of bijections from one or more elemental warpings that we term *units*. In Section 3.1 we give a general overview of the model; in Section 3.2 we describe the units; in Section 3.3 we describe the spatial process at the top layer; and in Sections 3.4 and 3.5 we discuss inference and prediction when the model is a spatial IWGP (SIWGP) and a spatial DSP (SDSP), respectively.

In this section we use the following notation for conciseness. Let  $\mathbf{b} \in \mathbb{R}^{d_1}$  denote a point in  $d_1$ -dimensional space, and  $\mathbf{B} \equiv (\mathbf{b}_1, \dots, \mathbf{b}_N)$  a collection of  $N$  points on the same space. Let  $h : \mathbb{R}^{d_1} \rightarrow \mathbb{R}$ , and  $\mathbf{h} \equiv (h_1, \dots, h_{d_2})'$  be a vector of  $d_2$  such mappings. We define  $h(\mathbf{B}) \equiv (h(\mathbf{b}_1), \dots, h(\mathbf{b}_N))$ ;  $\mathbf{h}(\mathbf{b}) \equiv (h_1(\mathbf{b}), \dots, h_{d_2}(\mathbf{b}))'$ ; and  $\mathbf{h}(\mathbf{B}) \equiv (\mathbf{h}(\mathbf{b}_1), \dots, \mathbf{h}(\mathbf{b}_N))$ . That is,  $h(\mathbf{B})$  returns a vector of size  $1 \times N$  containing the evaluation of  $h$  over the columns of  $\mathbf{B}$ ;  $\mathbf{h}(\mathbf{b})$  returns a vector of size  $d_2 \times 1$  containing the evaluations of  $h_i$  at  $\mathbf{b}$ , for  $i = 1, \dots, d_2$ ; and  $\mathbf{h}(\mathbf{B})$  returns a  $d_2 \times N$  matrix containing the function evaluations of  $\mathbf{h}$  at all the input locations in  $\mathbf{B}$ .

### 3.1 Model overview

The deep compositional spatial model we propose is constructed from several layers that (i) model the observed data conditional on the underlying process, (ii) model the process on the warped domain, and (iii) bijectively warp the geographic domain. In this work we use the observation model given in (1), although it is possible to consider other, non-Gaussian, likelihoods. The process layer is modelled as a low-rank process using basis functions which, as is common in geostatistical applications, are assumed to be fixed and known a priori. The process model is thus given by  $Y(\mathbf{s}) = \mathbf{w}'_{n+1} \boldsymbol{\phi}_{n+1}(\mathbf{f}(\mathbf{s}))$ ,  $\mathbf{s} \in G$ , and is described in more detail in Section 3.3.

Similar to several of the models described in Section 2, the warping layers are also modelled as low-rank processes. However, in light of our modelling choice of the top layer, we use basis functions which are fixed and known. Such a choice simplifies the estimation problem considerably, but also introduces the requirement that the domain at each layer is bounded and fixed a priori. Without loss of generalisation, we henceforth fix  $D_i = [c_1, c_2]^{d_i}, i = 1, \dots, n$ , where  $c_2 - c_1 = 1$  and  $c_1, c_2 \in \mathbb{R}$ . Our model thus differs slightly from those discussed in Section 2 in that the outputs of each layer are (linearly) rescaled before being input into the following layer. Note that bijectivity is retained under the individual rescaling of each output dimension. The parameters of these rescalings are computed at each layer by ensuring that the  $i$ th warping of a set of  $m$  input knots  $\tilde{\mathbf{F}}_0 \equiv \tilde{\mathbf{S}}$ , which we denote as  $\tilde{\mathbf{F}}_i$ , are interior or boundary points of  $D_i$ , for  $i = 1, \dots, n$ .

Let  $f_{ik}^u(\cdot) \equiv \mathbf{w}_i^{(k)'} \phi_i(\cdot)$  be the unscaled  $k$ th output of the  $i$ th layer, and let  $g_{ik}(f_{ik}^u(\cdot); \tilde{\mathbf{F}}_{i-1})$  denote the respective scaling function. The scaling function we use takes the form

$$g_{ik}(f_{ik}^u(\cdot); \tilde{\mathbf{F}}_{i-1}) \equiv \frac{f_{ik}^u(\cdot) - \min(f_{ik}^u(\tilde{\mathbf{F}}_{i-1}))}{\max(f_{ik}^u(\tilde{\mathbf{F}}_{i-1})) - \min(f_{ik}^u(\tilde{\mathbf{F}}_{i-1}))} + c_1, \quad (3)$$

where  $f_{ik}^u(\tilde{\mathbf{F}}_{i-1}) = \mathbf{w}_i^{(k)'} \phi_i(\tilde{\mathbf{F}}_{i-1})$  and  $\phi_i(\tilde{\mathbf{F}}_{i-1})$  is an  $r_i \times m$  matrix of basis function evaluated at the knot locations. Hence,  $f_{ik}^u(\tilde{\mathbf{F}}_{i-1})$  is a vector of warped locations, and  $\min(\cdot)$  and  $\max(\cdot)$  return the minimum and maximum of these locations, respectively. At each warping layer we collect the  $d_i$  scaling functions into the vector  $\mathbf{g}_i(\mathbf{f}_i^u(\cdot); \tilde{\mathbf{F}}_{i-1}) \equiv (g_{ik}(f_{ik}^u(\cdot); \tilde{\mathbf{F}}_{i-1})) : k = 1, \dots, d_i'$ . The input knots,  $\tilde{\mathbf{S}}$ , should be representative of the spatial extent of the observed data on  $G$ ,  $\mathbf{S} \equiv (\mathbf{s}_1, \dots, \mathbf{s}_N)$ . For simplicity (and this is what we do in our implementation) one can construct  $\tilde{\mathbf{S}}$  from the set of unique observation locations. Note that  $g_{ik}(f_{ik}^u(\cdot); \tilde{\mathbf{F}}_{i-1})$  is invariant to linear scalings of  $f_{ik}^u(\cdot)$ , and hence of  $\mathbf{w}_i^{(k)}$ . Issues with non-identifiability of this kind can be easily resolved by using ridge regression when doing maximum-likelihood estimation, or through the use of appropriate prior distributions when doing Bayesian inference.

In summary, our deep compositional spatial model has the following hierarchical structure:

$$\begin{aligned} \text{Observation model: } Z(\mathbf{s}_i) &= Y(\mathbf{s}_i) + \epsilon_i, \quad i = 1, \dots, N, \\ \text{Top-layer process model: } Y(\mathbf{s}) &= \mathbf{w}'_{n+1} \phi_{n+1}(\mathbf{f}(\mathbf{s})), \quad \mathbf{s} \in G \\ &\mathbf{f}_n(\mathbf{s}) = \mathbf{g}_n(\mathbf{W}_n \phi_n(\mathbf{s}; \Theta_n); \tilde{\mathbf{F}}_{n-1}), \quad \mathbf{s} \in D_{n-1}, \\ \text{Warping process models: } &\vdots \\ &\mathbf{f}_1(\mathbf{s}) = \mathbf{g}_1(\mathbf{W}_1 \phi_1(\mathbf{s}; \Theta_1); \tilde{\mathbf{S}}), \quad \mathbf{s} \in G. \end{aligned}$$

In Section 3.2 we describe specific forms of  $\mathbf{f}_i^u(\cdot) \equiv (f_{ik}^u(\cdot) : k = 1, \dots, d_i)'$ ,  $i = 1, \dots, n$  that, through composition, can define flexible bijective warpings.

## 3.2 Warping units

### Axial warping units

An axial warping unit (AWU) is a nonlinear mapping of one of the input dimensions. The map is constrained to be monotonic, and hence bijective. The AWU at the  $i$ th layer has  $d_{i-1}$  inputs and  $d_i = d_{i-1}$  outputs. Only one of the inputs is warped, while the others are simply forwarded on to the following layer. In particular, we define an AWU that warps the  $k$ th input dimension as follows:

$$\begin{aligned} f_{ik}^u(\mathbf{s}) &= \mathbf{w}_i^{(k)'} \boldsymbol{\phi}_i(\mathbf{s}; \boldsymbol{\Theta}_i), \quad \mathbf{s} \in D_{i-1}, \\ f_{ik'}^u(\mathbf{s}) &= s_{k'}, \quad k' \neq k, \mathbf{s} \in D_{i-1}, \end{aligned}$$

where  $\phi_{i1}(\mathbf{s}; \theta_{i1}) = s_k$  and

$$\phi_{ij}(\mathbf{s}; \boldsymbol{\theta}_{ij}) = \text{sig}(s_k; \boldsymbol{\theta}_{ij}) \equiv \frac{1}{1 + \exp(-\theta_{ij1}(s_k - \theta_{ij2}))}, \quad j = 2, \dots, r_i. \quad (4)$$

The first basis function models a linear scaling, while the  $\{\phi_{ij}(\cdot; \boldsymbol{\theta}_{ij}) : j = 2, \dots, r_i\}$  are sigmoid functions that model nonlinear scaling. The monotonicity of the sigmoid functions ensure that if  $\mathbf{w}_i^{(k)}$  is nonnegative,  $f_{ik}^u(\mathbf{s})$ , and hence  $\mathbf{f}_i^u(\mathbf{s})$ , is bijective. In the SIWGP, the nonnegativity can be guaranteed by estimating the transformed parameters  $\{\log(w_{ikj})\}$  and then transforming back through the exponential function. In the SDSP, bijectivity of the sample paths can be ensured by letting the weights have a lognormal prior distribution, that is, by letting  $\tilde{w}_{ijk} = \log(w_{ikj}) \sim \text{Gau}(\mu_{ijk}, \sigma_{ijk}^2)$ .

We fix the parameters  $\boldsymbol{\Theta}_i \equiv (\theta_{i21}, \theta_{i22}, \theta_{i31}, \dots, \theta_{ir_i2})'$  such that  $\{\phi_{ij}(\cdot; \boldsymbol{\theta}_{ij}) : j = 2, \dots, r_i\}$  can reproduce a wide range of smooth warping functions over the entire input domain,  $D_{i-1}$ . This is feasible in the low dimensional settings of spatial applications, and results in a considerably streamlined inference problem with little loss in model representation. The resulting formulation is also intuitive:  $f_{ik}^u(\cdot)$  results in little warping when all the unknown weights except the first are close to zero, while a large non-negative weight on one of the sigmoid functions will result in local relative stretching out of the input domain.

As an illustration of the AWU, consider the identity function and the 11 sigmoid functions in the interval  $[0, 1]$  shown in Figure 1, top panel. The bottom two panels of Figure 1 show the warping function and the effect on an input signal equal to  $\sin(50s)$  when (left panels) all basis-function coefficients are zero except for the fifth (from left to right), which is equal to 1, (middle panels) the basis-function coefficients increase cubically (from left to right) from 0 to 1 and (right panels) the basis-function coefficients decrease cubically (from left to right) from 1 to 0. In all cases, the output shown is that of the AWU rescaled to the interval  $[0, 1]$ . An AWU formed from several basis functions can be much more flexible than one constructed using a Beta CDF (Snoek et al., 2014); it is also likely easier to fit since the inference problem does not require basis-function parameter estimation, but only the estimation of a set of nonnegative weights which have local spatial scope.

### RBF units

RBFs from  $\mathbb{R}^2$  to  $\mathbb{R}^2$  can be used to describe local expansions/contractions, and can warp at various resolutions. A single resolution RBF (SR-RBF) unit is formed from a composition

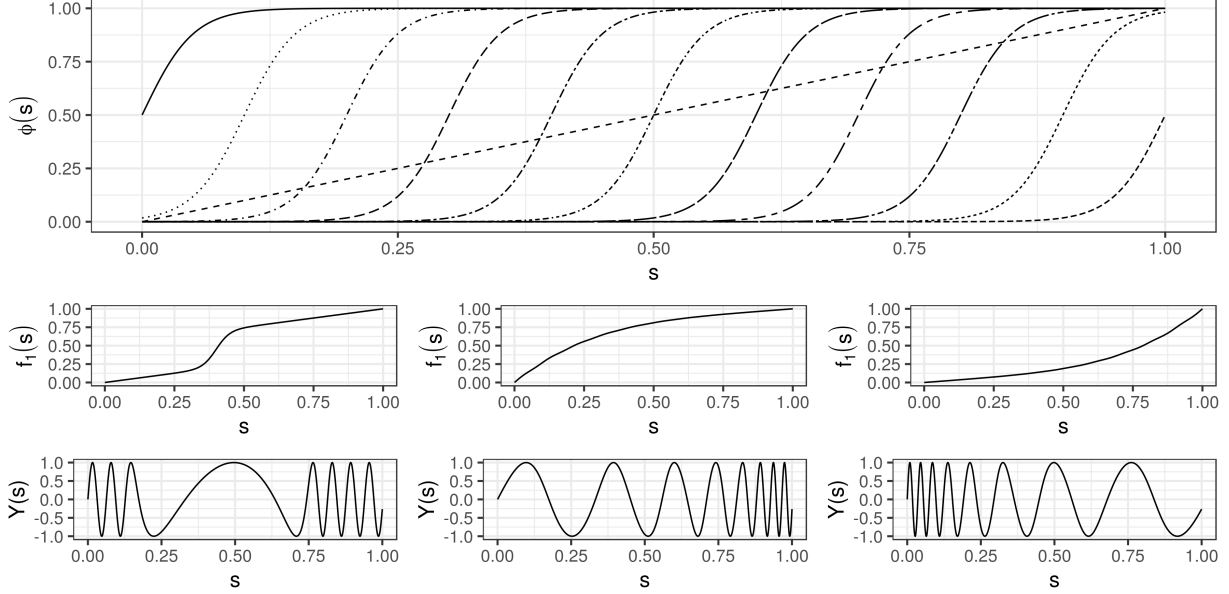


Figure 1: The axial warping unit. Top panel: The identity map and 11 sigmoid functions regularly spaced on the interval  $[0, 1]$ . Centre panels: Three different realisations of axial warping units reflective of different combinations of sigmoid-basis-function coefficients (see main text for details). Bottom panels: The output from an axial warping unit when the input is equal to  $\sin(50s)$  for  $s \in [0, 1]$ .

of the RBFs of Perrin and Monestiez (1999), given by (2).

It is straightforward to see that one can re-express Perrin and Monestiez’s RBF warping as a weighted sum of basis functions. In particular,

$$\mathbf{f}_i^u(\mathbf{s}) = \mathbf{W}_i \phi_i(\mathbf{s}; \Theta_i), \quad \mathbf{s} \in D_{i-1},$$

where  $\phi_{i1}(\mathbf{s}) = s_1$ ,  $\phi_{i2}(\mathbf{s}) = s_2$ ,  $\phi_{i3}(\mathbf{s}; \Theta_i) = \psi_{i1}(\mathbf{s}; \Theta_i)$ , and  $\phi_{i4}(\mathbf{s}; \Theta_i) = \psi_{i2}(\mathbf{s}; \Theta_i)$ , where  $\psi_{ij}(\mathbf{s}; \Theta_i) = (s_j - \gamma_{ij}) \exp(-a_i \|\mathbf{s} - \gamma_i\|^2)$ ,  $\mathbf{s} \in D_{i-1}$ ,  $j = 1, 2$ , and  $\Theta_i \equiv (\gamma_i', a_i)'$ . The weight matrix has the form  $\mathbf{W}_i = [\mathbf{I} w_i \mathbf{I}]$ , so that only one weight  $w_i$  needs to be estimated per layer (since, as with the AWUs, we fix  $\Theta_i$ ). Importantly, it is required that  $-1 < w_i < \exp(3/2)/2$  for each  $i$  to enforce bijectivity (Perrin and Monestiez, 1999).

The parameters  $\Theta_i$  are fixed in such a way that an SR-RBF unit can smoothly warp the entire domain, with higher resolutions able to provide more detailed and complex deformations. In our setup we let the  $l$ th resolution have RBFs arranged on a  $3^l \times 3^l$  grid, so that at the  $l$ th resolution the SR-RBF unit has  $3^{2l}$  layers. The scale parameter of the RBFs should increase with resolution. On  $[0, 1] \times [0, 1]$  we set  $a_i = 2 \cdot (3^l - 1)^2$  (where  $i$  is the layer corresponding to the RBF); this choice results in the  $\exp(-1/2)$  contour lines of squared-exponential components of the RBFs intersecting with those of their neighbours at a single point.

In an SIWGP, the constraint on  $w_i$  can be achieved by estimating the transformed parameter  $\tilde{w}_i$  without any constraints, where  $\tilde{w}_i = \text{logit}((1 + w_i)/(1 + \exp(3/2)/2))$ . In an SDSP we equip  $\tilde{w}_i$  with a Gaussian distribution, that is, we let  $\tilde{w}_i \sim \text{Gau}(\mu_i, \sigma_i^2)$ . Note

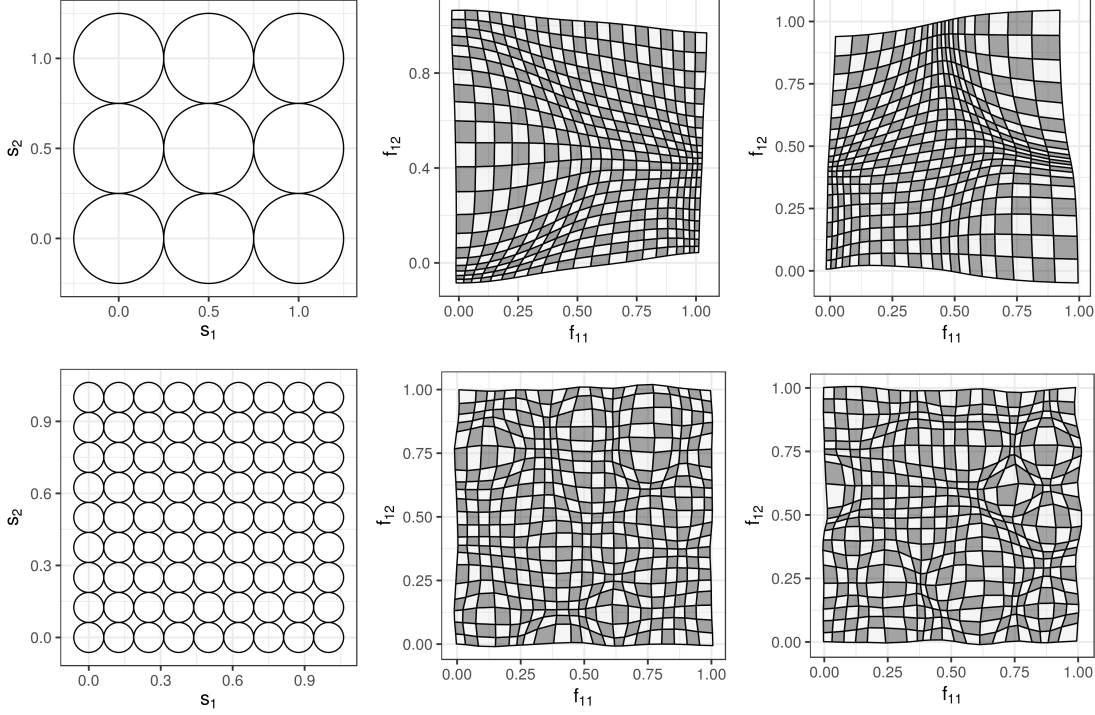


Figure 2: Single-resolution RBF (SR-RBF) units (left panels) and random realisations of warpings of regular chequered patterns on  $[0, 1]^2$  from these units (centre and right panels). Top panels: Resolution  $l = 1$ , where the RBFs are arranged on a  $3 \times 3$  grid and  $a_i = 8$ . Bottom panels: Resolution  $l = 2$ , where the RBFs are arranged on a  $9 \times 9$  grid and  $a_i = 128$ .

that when  $w_i = 0$  ( $\tilde{w}_i \approx -0.8$ ),  $\mathbf{f}_i^u(\mathbf{s}) = (s_1, s_2)'$ ,  $\mathbf{s} \in D_{i-1}$ , that is, the input to the layer is not warped. We therefore set  $\mu_i = -0.8$ .

In Figure 2 we show two resolutions of RBFs, and an example of warpings that can be generated using these basis functions, with the output rescaled to the unit square  $[0, 1] \times [0, 1]$ . We stress that unlike the AWUs, these RBFs are combined through composition and not summation in order to ensure bijectivity of the composite map. As in the case of spatial processes (e.g., Cressie and Johannesson, 2008; Nychka et al., 2015), we expect warpings to occur at various scales. We can model these multi-resolutional warpings through the composition of two or more SR-RBFs at different resolutions. We denote an SR-RBF at the  $l$ th resolution as SR-RBF( $l$ ).

### Möbius transformation units

Möbius transformations are bijective mappings from the complex plane,  $\mathbb{C}$ , to itself (which, for the purposes of this work, can be seen as a map from  $\mathbb{R}^2$  to  $\mathbb{R}^2$ ). Define  $z(\mathbf{s}) \equiv s_1 + s_2\iota$ , where  $\iota \equiv \sqrt{-1}$ , and let  $\mathbf{a} \in \mathbb{C}^4$ . Then, the Möbius transformation is given by  $\phi_i^m(z(\mathbf{s}); \Theta_i) = (a_1z(\mathbf{s}) + a_2)/(a_3z(\mathbf{s}) + a_4)$ , where  $\Theta_i \equiv (a_1, \dots, a_4)'$ . This warping unit contains 8 unknown parameters (the real and imaginary components of  $\mathbf{a}$ ) and all weights

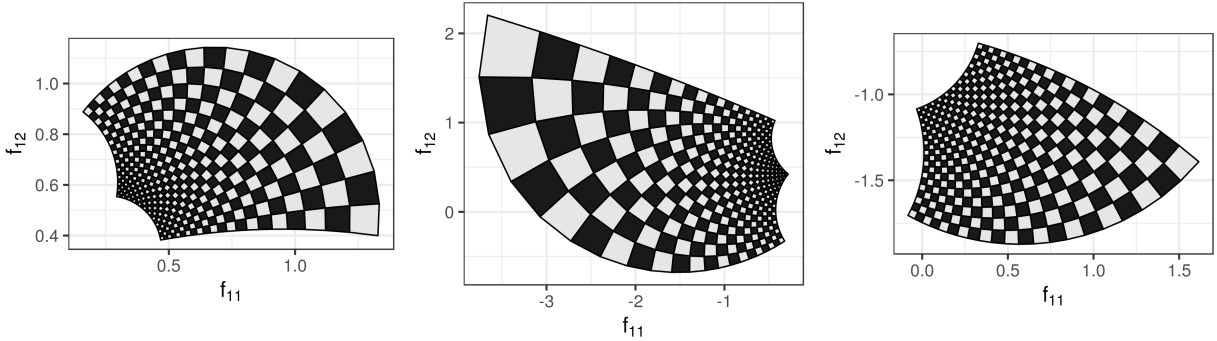


Figure 3: Möbius transformations of regular chequered patterns, obtained by randomly generating the real and imaginary components of  $\mathbf{a} \in \mathbb{C}^4$  from a standard normal distribution subject to the constraint that  $-a_4/a_3$  is not in the unit square enclosed by the points  $0 + 0\iota, 0 + 1\iota, 1 + 1\iota, 1 + 0\iota$  on the complex plane.

are fixed to one. That is,

$$\begin{aligned} f_{i1}^u(\mathbf{s}) &= \text{Re}(\phi_i^m(z(\mathbf{s}); \Theta_i)), & \mathbf{s} \in D_{i-1}, \\ f_{i2}^u(\mathbf{s}) &= \text{Im}(\phi_i^m(z(\mathbf{s}); \Theta_i)), & \mathbf{s} \in D_{i-1}, \end{aligned}$$

where  $\text{Re}(\cdot)$  and  $\text{Im}(\cdot)$  return the real and imaginary components of their arguments, respectively. The Möbius transformation unit is distinct from the units considered so far, in that it does not have any weights that need to be estimated, but contains a set of parameters that do need to be.

It is easy to show that a Möbius transformation of a Möbius transformation is itself a Möbius transformation and therefore there is no benefit in cascading more than one of these transformation units in immediate sequence (although there could be some benefit in having them intermittently throughout the network, separated by other warping units). The unit maps  $\mathbf{s}$  to infinity for  $z(\mathbf{s}) = -a_4/a_3$  and we therefore need to ensure that the spatial coordinates implied by the complex number  $-a_4/a_3$  are not in  $D_{i-1}$ . Assuming that  $D_{i-1} = [0, 1] \times [0, 1]$ , this is equivalent to asserting that the real or imaginary component of  $-a_4/a_3$  is outside of the interval  $[0, 1]$ , something that can be ensured when optimising  $\Theta_i$ . Note that  $a_2 = a_3 = 0$  and  $a_1 = a_4 = 1$  implies no transformation. Figure 3 shows three random Möbius transformations, where all components of  $\mathbf{a}$  were simulated from a standard normal distribution subject to the above constraint.

### 3.3 The top-level spatial process

The top  $(n + 1)$ th layer of the deep compositional spatial model is defined through the process  $Y(\cdot)$ . To deal with moderately large datasets, we choose to have a low-rank representation for  $Y(\cdot)$ . Specifically, we let

$$Y(\mathbf{s}) = \mathbf{w}'_{n+1} \phi_{n+1}(\mathbf{s}; \Theta_{n+1}), \quad \mathbf{s} \in D_n,$$

where the random weights  $\mathbf{w}_{n+1}$  have a Gaussian distribution with some mean  $\boldsymbol{\mu}$  (which henceforth we take equal to  $\mathbf{0}$  without loss of generality) and covariance matrix  $\boldsymbol{\Sigma}_{\tau_{n+1}}$ ,  $\boldsymbol{\tau}_{n+1}$  is a vector of unknown parameters appearing in  $\boldsymbol{\Sigma}_{\tau_{n+1}}$ , and the basis functions  $\phi_{n+1}(\cdot; \boldsymbol{\Theta}_{n+1})$  take inputs in  $D_n \subset \mathbb{R}^{d_n}$ . Such a model is feasible when  $d_n$  is small, say  $d_n \leq 4$ , as is typical in spatial applications.

In our implementation we let  $\phi_{n+1}(\cdot; \boldsymbol{\Theta}_{n+1})$  be a set of bisquare basis functions. That is, we let

$$\phi_{n+1,j}(\mathbf{s}; \boldsymbol{\theta}_{n+1,j}) \equiv \begin{cases} \{1 - (\|\mathbf{s} - \boldsymbol{\gamma}_{n+1,j}\|/\delta_{n+1,j})^2\}^2; & \|\mathbf{s} - \boldsymbol{\gamma}_{n+1,j}\| \leq \delta_{n+1,j} \\ 0; & \text{otherwise,} \end{cases}$$

where the parameter vector  $\boldsymbol{\theta}_{n+1,j} \equiv (\boldsymbol{\gamma}'_{n+1,j}, \delta_{n+1,j})'$  is made up of the centroid  $\boldsymbol{\gamma}_{n+1,j}$  and the aperture  $\delta_{n+1,j}$ . We let the bisquare basis functions  $\phi_{n+1}(\cdot; \boldsymbol{\Theta}_{n+1})$  be regularly distributed in  $D_n$  and model the covariances of the weights as  $\boldsymbol{\Sigma}_{\tau_{n+1}} = (\sigma^2 \exp(-\|\boldsymbol{\gamma}_{n+1,j} - \boldsymbol{\gamma}_{n+1,j'}\|/l)) : j, j' = 1, \dots, r_{n+1}$  (see Zammit-Mangion and Cressie, 2019, for more details) where  $\boldsymbol{\tau}_{n+1} = (\sigma^2, l)'$ . Note that this top-level spatial process is not stationary, but is usually able to approximate stationary processes reasonably well. Similar models that can deal with a larger number of basis functions, and where instead a sparse precision matrix  $\mathbf{Q}_{\tau_{n+1}}$  is modelled (e.g., Lindgren et al., 2011; Nychka et al., 2015), are left for future consideration (see Section 5).

The top-layer process thus completes our specification of the deep compositional spatial model outlined in Section 3.1. In Sections 3.4 and 3.5 we discuss inference schemes for when the deep spatial model is an SIWGP and an SDSF, respectively.

### 3.4 Inference for SIWGPs

In SIWGPs and SDSFs, inference needs to be made on both the weights and the parameters. In order to render the optimisation problem on the weights unconstrained, we often transform the weights; further, this transformation is dependent on the layer type. Recall that the transformation is a log function when the layer is an AWU, a logit function when the layer is an RBF unit, and the identity when the layer is a Möbius transformation. Denote the weights-transformation functions as  $h_i(\cdot)$ ,  $i = 1, \dots, n$ , which are monotonic and invertible. Then, inference on the weights is a by-product of making inference on the transformed weights  $\widetilde{\mathbf{W}}_i = h_i(\mathbf{W}_i)$ ,  $i = 1, \dots, n$ .

In SIWGPs, all unknowns in the set of transformed weights  $\widetilde{\mathbf{W}}_n \equiv \{\widetilde{\mathbf{W}}_1, \dots, \widetilde{\mathbf{W}}_n\}$  and the set of parameters  $\boldsymbol{\Theta}_n \equiv \{\boldsymbol{\Theta}_1, \dots, \boldsymbol{\Theta}_n\}$  appearing in the warping model, as well as the process-model parameters  $\boldsymbol{\tau}_{n+1}$  and the measurement-model noise variance  $\sigma_\epsilon^2$ , are estimated using maximum likelihood. (Recall that several of the components of  $\boldsymbol{\Theta}_n$  are in fact known and fixed by assumption). We collect the warping weights and parameters into the set  $\underline{\mathbf{A}} \equiv \{\widetilde{\mathbf{W}}_n, \boldsymbol{\Theta}_n\}$ . Inference needs to be made on the process  $Y(\cdot)$  through  $\mathbf{W}_{n+1} = \mathbf{w}_{n+1}$  (which is random) by conditioning on the noisy data.

Let  $\mathbf{Z} \equiv (Z(\mathbf{s}_1), \dots, Z(\mathbf{s}_N))'$  denote the observed data and  $\mathbf{Y} \equiv (Y(\mathbf{s}_1), \dots, Y(\mathbf{s}_N))'$  the latent process at the locations  $\mathbf{s}_1, \dots, \mathbf{s}_N \in G$ . Then  $\mathbf{Z} = \mathbf{A}_{\underline{\mathbf{A}}} \mathbf{w}_{n+1} + \boldsymbol{\epsilon}$ , where  $\mathbf{A}_{\underline{\mathbf{A}}} \equiv (\phi_{n+1}(\mathbf{f}(\mathbf{s}_i; \underline{\mathbf{A}}); \boldsymbol{\Theta}_{n+1}) : i = 1, \dots, N)'$  and  $\boldsymbol{\epsilon} \equiv (\epsilon_i : i = 1, \dots, N)'$ . Recall that  $\mathbf{f} \equiv$

$\mathbf{f}_n \circ \mathbf{f}_{n-1} \circ \dots \circ \mathbf{f}_1$ , and it therefore depends on all of  $\underline{\mathbf{A}}$ . Omitting the dependence on  $\Theta_{n+1}$ , which is fixed by assumption, the marginal, or integrated, likelihood is

$$p(\mathbf{Z} \mid \underline{\mathbf{A}}, \tau_{n+1}, \sigma_\epsilon^2) = \int p(\mathbf{Z} \mid \mathbf{w}_{n+1}, \underline{\mathbf{A}}, \sigma_\epsilon^2) p(\mathbf{w}_{n+1} \mid \tau_{n+1}) d\mathbf{w}_{n+1},$$

which can be written out as

$$\begin{aligned} \log p(\mathbf{Z} \mid \underline{\mathbf{A}}, \tau_{n+1}, \sigma_\epsilon^2) = \text{const.} & - \frac{N}{2} \log \sigma_\epsilon^2 - \frac{1}{2} \log |\Sigma_{\tau_{n+1}}| - \frac{1}{2} \log \left| \frac{1}{\sigma_\epsilon^2} \mathbf{A}'_{\underline{\mathbf{A}}} \mathbf{A}_{\underline{\mathbf{A}}} + \Sigma_{\tau_{n+1}}^{-1} \right| - \\ & \frac{1}{2} \mathbf{Z}' \left[ \frac{1}{\sigma_\epsilon^2} \mathbf{I} - \frac{1}{\sigma_\epsilon^4} \mathbf{A}_{\underline{\mathbf{A}}} \left( \frac{1}{\sigma_\epsilon^2} \mathbf{A}'_{\underline{\mathbf{A}}} \mathbf{A}_{\underline{\mathbf{A}}} + \Sigma_{\tau_{n+1}}^{-1} \right)^{-1} \mathbf{A}'_{\underline{\mathbf{A}}} \right] \mathbf{Z}. \end{aligned} \quad (5)$$

Estimates of  $\underline{\mathbf{A}}$ ,  $\tau_{n+1}$  and  $\sigma_\epsilon^2$  ( $\hat{\underline{\mathbf{A}}}$ ,  $\hat{\tau}_{n+1}$  and  $\hat{\sigma}_\epsilon^2$ , respectively), can be found using gradient-based optimisation. Note that (3) is not differentiable everywhere with respect to the weights on the original scale; specifically, it is not differentiable along a finite number of hyperplanes that satisfy  $\mathbf{w}_i^{(k)'} \mathbf{v} = 0$  where  $\mathbf{v}$  depends on the chosen knots. Since these hyperplanes occupy an infinitesimally small volume in the vector space of  $\mathbf{w}_i^{(k)}$ , they are almost certainly never going to be coincident with an estimate of  $\mathbf{w}_i^{(k)}$  in a gradient descent. Differentiable approximations to the maximum and minimum functions are available if desired (e.g., Lange et al., 2014).

In our implementation, gradients were found using automatic differentiation (AD), where the gradients of (5) with respect to the unknown weights and parameters are computed during runtime using, for example, back propagation (Goodfellow et al., 2016, Section 6.5). AD obviates the need for analytical gradient computation, and has gained considerable interest in recent years through its use in the popular statistical modelling and fitting packages **Stan**, **Greta**, and **TMB**. For this work we employed the AD functionality in the library **TensorFlow** (Abadi et al., 2015) through **R** (R Core Team, 2018; Allaire and Tang, 2018).

## Prediction

Once  $\underline{\mathbf{A}}$ ,  $\tau_{n+1}$ , and  $\sigma_\epsilon^2$  are estimated, they are used for prediction. Specifically, for a set of  $N^*$  prediction locations on  $G$ ,  $\mathbf{s}_j^*$ ,  $j = 1, \dots, N^*$ , define  $\mathbf{Y}^* \equiv (Y(\mathbf{s}_j^*) : j = 1, \dots, N^*)'$ . The prediction and prediction variance of  $\mathbf{Y}^*$  are

$$E(\mathbf{Y}^* \mid \mathbf{Z}, \hat{\underline{\mathbf{A}}}, \hat{\tau}_{n+1}, \hat{\sigma}_\epsilon^2) = \mathbf{A}_{\hat{\underline{\mathbf{A}}}}^* \boldsymbol{\mu}_{n+1}^*, \quad \text{and} \quad (6)$$

$$\text{Var}(\mathbf{Y}^* \mid \mathbf{Z}, \hat{\underline{\mathbf{A}}}, \hat{\tau}_{n+1}, \hat{\sigma}_\epsilon^2) = \mathbf{A}_{\hat{\underline{\mathbf{A}}}}^* \Sigma_{n+1}^* \mathbf{A}_{\hat{\underline{\mathbf{A}}}}^{*'}, \quad (7)$$

respectively, where  $\mathbf{A}_{\hat{\underline{\mathbf{A}}}}^* \equiv (\phi_{n+1}(\mathbf{f}(\mathbf{s}_j^*; \hat{\underline{\mathbf{A}}}); \Theta_{n+1}) : j = 1, \dots, N^*)'$ , and

$$\Sigma_{n+1}^{*-1} = \frac{1}{\hat{\sigma}_\epsilon^2} \mathbf{A}'_{\hat{\underline{\mathbf{A}}}} \mathbf{A}_{\hat{\underline{\mathbf{A}}}} + \Sigma_{\hat{\tau}_{n+1}}^{-1}, \quad (8)$$

$$\boldsymbol{\mu}_{n+1}^* = \frac{1}{\hat{\sigma}_\epsilon^2} \Sigma_{n+1}^* \mathbf{A}'_{\hat{\underline{\mathbf{A}}}} \mathbf{Z}, \quad (9)$$

are the precision and expectation of the weights  $\mathbf{w}_{n+1}$  when conditioned on the data  $\mathbf{Z}$  and the estimated quantities  $\hat{\underline{\mathbf{A}}}$ ,  $\hat{\tau}_{n+1}$ , and  $\hat{\sigma}_\epsilon^2$ .

### 3.5 Inference for SDSPs

In SDSPs, the transformed weight vectors in the  $i$ th layer,  $\{\tilde{\mathbf{w}}_i^{(k)} : k = 1, \dots, d_i\}$ , are equipped with multivariate Gaussian distributions with means  $\boldsymbol{\mu}_i$  (such that the prior mean is reflective of no, or little, warping), and covariance matrix  $\sigma_i^2 \mathbf{I}$ . In our implementation, we fixed  $\sigma_i^2$  to a large value for each  $i$  to keep these prior distributions diffuse. The parameters  $\{\sigma_i^2\}$  could instead be estimated or fixed to small values to add soft limits to the intensity of the warpings in the hidden layers.

As with DGPs, inference with the SDSP is generally a difficult problem since  $\log p(\mathbf{Z} | \widetilde{\mathbf{W}}_n, \boldsymbol{\Theta}_n, \boldsymbol{\tau}_{n+1}, \sigma_\epsilon^2)$  is a highly nonlinear function of  $\widetilde{\mathbf{W}}_n$ . Hence, marginalisation of  $\widetilde{\mathbf{W}}_n$  is not possible analytically, and one cannot easily compute expectations with respect to  $\widetilde{\mathbf{W}}_n | \mathbf{Z}, \boldsymbol{\Theta}_n, \boldsymbol{\tau}_{n+1}, \sigma_\epsilon^2$ . This renders the use of expectation-maximisation inference frameworks difficult to implement for SDSP models.

Here, we instead employ an approximate Bayesian framework, variational Bayes (VB), with the aim of finding an approximate posterior distribution to  $p(\widetilde{\mathbf{W}}_n | \mathbf{Z}, \boldsymbol{\Theta}_n, \boldsymbol{\tau}_{n+1}, \sigma_\epsilon^2)$ , which we denote as  $q(\widetilde{\mathbf{W}}_n)$ , whose form we specify later. In VB, the marginal likelihood is first bounded, and the lower bound is then maximised with respect to the parameters appearing in  $q(\widetilde{\mathbf{W}}_n)$ , as well as  $\boldsymbol{\Theta}_n, \boldsymbol{\tau}_{n+1}$ , and  $\sigma_\epsilon^2$ . For excellent introductions to the VB approach to approximating intractable posterior distributions, see Beal (2003, Chapter 2), Bishop (2006, Chapter 10), and Blei et al. (2017).

Consider the set of spatial locations of the data on  $G$ ,  $\mathbf{S} \equiv (\mathbf{s}_1, \dots, \mathbf{s}_N) \equiv \mathbf{F}_0$ . The function outputs at the first layer from the inputs  $\mathbf{S}$  are  $\mathbf{F}_1 = (\mathbf{f}_1(\mathbf{s}_1), \dots, \mathbf{f}_1(\mathbf{s}_N))$ , which, recall, we write as  $\mathbf{f}_1(\mathbf{S})$  for conciseness. Similarly, the outputs at the  $i$ th layer are  $\mathbf{F}_i = \mathbf{f}_i(\mathbf{F}_{i-1})$ . Collect all these warped variables into  $\underline{\mathbf{F}}_n \equiv \{\mathbf{F}_1, \dots, \mathbf{F}_n\}$  and assume that the matrix  $\tilde{\mathbf{S}}$  consists of some or all of the columns of  $\mathbf{S}$ , so that  $\tilde{\mathbf{F}}_i$  also consists of some or all of the columns of  $\mathbf{F}_i$ ,  $i = 1, \dots, n$ . (This latter assumption removes the need for defining separate variational distributions over the knots.) Our marginal likelihood is (again, ignoring the dependence on  $\boldsymbol{\Theta}_{n+1}$ , which is fixed by assumption)

$$\begin{aligned}
& \log p(\mathbf{Z} | \boldsymbol{\Theta}_n, \boldsymbol{\tau}_{n+1}, \sigma_\epsilon^2) \\
&= \log \int p(\mathbf{Z} | \underline{\mathbf{F}}_n, \widetilde{\mathbf{W}}_n, \boldsymbol{\Theta}_n, \boldsymbol{\tau}_{n+1}, \sigma_\epsilon^2) p(\underline{\mathbf{F}}_n, \widetilde{\mathbf{W}}_n | \boldsymbol{\Theta}_n) d\underline{\mathbf{F}}_n d\widetilde{\mathbf{W}}_n \\
&= \log \int q(\underline{\mathbf{F}}_n, \widetilde{\mathbf{W}}_n | \boldsymbol{\Theta}_n) \frac{p(\mathbf{Z} | \underline{\mathbf{F}}_n, \widetilde{\mathbf{W}}_n, \boldsymbol{\Theta}_n, \boldsymbol{\tau}_{n+1}, \sigma_\epsilon^2) p(\underline{\mathbf{F}}_n, \widetilde{\mathbf{W}}_n | \boldsymbol{\Theta}_n)}{q(\underline{\mathbf{F}}_n, \widetilde{\mathbf{W}}_n | \boldsymbol{\Theta}_n)} d\underline{\mathbf{F}}_n d\widetilde{\mathbf{W}}_n \\
&\geq E_{q(\underline{\mathbf{F}}_n, \widetilde{\mathbf{W}}_n | \boldsymbol{\Theta}_n)} \left[ \log \frac{p(\mathbf{Z} | \underline{\mathbf{F}}_n, \widetilde{\mathbf{W}}_n, \boldsymbol{\Theta}_n, \boldsymbol{\tau}_{n+1}, \sigma_\epsilon^2) p(\underline{\mathbf{F}}_n, \widetilde{\mathbf{W}}_n | \boldsymbol{\Theta}_n)}{q(\underline{\mathbf{F}}_n, \widetilde{\mathbf{W}}_n | \boldsymbol{\Theta}_n)} \right] \equiv \mathcal{E}, \quad (10)
\end{aligned}$$

by Jensen's inequality. Now,  $\mathbf{Z}$  is conditionally independent of  $\widetilde{\mathbf{W}}_n, \underline{\mathbf{F}}_{n-1}$ , and  $\boldsymbol{\Theta}_n$  when conditioned on  $\underline{\mathbf{F}}_n$ , and hence the likelihood  $p(\mathbf{Z} | \underline{\mathbf{F}}_n, \widetilde{\mathbf{W}}_n, \boldsymbol{\Theta}_n, \boldsymbol{\tau}_{n+1}, \sigma_\epsilon^2) = p(\mathbf{Z} | \underline{\mathbf{F}}_n, \boldsymbol{\tau}_{n+1}, \sigma_\epsilon^2)$ . This term is identical to (5) with  $\mathbf{A}_\Delta$  replaced with  $\boldsymbol{\phi}_{n+1}(\underline{\mathbf{F}}_n; \boldsymbol{\Theta}_{n+1})'$ .

Unfortunately, free-form variational optimisation (where we do not specify the functional form of  $q(\underline{\mathbf{F}}_n, \widetilde{\mathbf{W}}_n | \boldsymbol{\Theta}_n)$ ) is not analytically tractable. Following the approach first used for the latent-variable Gaussian process (Titsias and Lawrence, 2010) and subsequently

for sparse DGPs (Damianou and Lawrence, 2013), we constrain  $q(\mathbf{F}_n, \widetilde{\mathbf{W}}_n \mid \underline{\Theta}_n)$  to take the form

$$q(\mathbf{F}_n, \widetilde{\mathbf{W}}_n \mid \underline{\Theta}_n) = p(\mathbf{F}_n \mid \widetilde{\mathbf{W}}_n, \mathbf{F}_{n-1}, \underline{\Theta}_n) \cdots p(\mathbf{F}_1 \mid \widetilde{\mathbf{W}}_1, \underline{\Theta}_1) q(\widetilde{\mathbf{W}}_n) \cdots q(\widetilde{\mathbf{W}}_1).$$

We further let  $q(\widetilde{\mathbf{W}}_i) = \prod_{k=1}^{d_i} q(\tilde{\mathbf{w}}_i^{(k)})$  where  $q(\tilde{\mathbf{w}}_i^{(k)}) = \text{Gau}(\mathbf{m}_i^{(k)}, \mathbf{V}_i^{(k)}(\boldsymbol{\eta}_i^{(k)}))$ ,  $i = 1, \dots, n$ . The covariance matrix of the variational distribution,  $\mathbf{V}_i^{(k)}(\boldsymbol{\eta}_i^{(k)})$ , is parameterised through its lower Cholesky factor. That is,  $\mathbf{V}_i^{(k)}(\boldsymbol{\eta}_i^{(k)}) = (\mathbf{L}_i^{(k)}(\boldsymbol{\eta}_i^{(k)}))(\mathbf{L}_i^{(k)}(\boldsymbol{\eta}_i^{(k)}))'$ , where

$$\mathbf{L}_i^{(k)}(\boldsymbol{\eta}_i^{(k)}) = \begin{pmatrix} e^{\eta_{i,11}^{(k)}} & & & & \\ \eta_{i,21}^{(k)} & e^{\eta_{i,22}^{(k)}} & & & \\ \eta_{i,31}^{(k)} & \eta_{i,32}^{(k)} & e^{\eta_{i,33}^{(k)}} & & \\ \vdots & \vdots & \vdots & \ddots & \end{pmatrix},$$

and where the exponential terms on the diagonal ensure that  $\mathbf{V}_i^{(k)}(\boldsymbol{\eta}_i^{(k)})$  is positive-definite. This Cholesky factor can be made sparse if desired (e.g., Tan and Nott, 2018).

Substituting our choice of  $q(\mathbf{F}_n, \widetilde{\mathbf{W}}_n \mid \underline{\Theta}_n)$  into (10) we obtain an expression for the lower bound

$$\mathcal{E} = E_{q(\mathbf{F}_n \mid \underline{\Theta}_n)} [\log p(\mathbf{Z} \mid \mathbf{F}_n, \boldsymbol{\tau}_{n+1}, \sigma_\epsilon^2)] - \sum_{i=1}^n KL(q(\widetilde{\mathbf{W}}_i) \parallel p(\widetilde{\mathbf{W}}_i)) \equiv \mathcal{E}_1 - \mathcal{E}_2,$$

where  $\mathcal{E}_1$  is the expected marginal log-likelihood (where the expectation is taken under the variational posterior distribution of the warped locations, defined below in (11)),  $\mathcal{E}_2$  is the sum of Kullback–Leibler divergences between the variational posterior distributions over  $\{\widetilde{\mathbf{W}}_i\}$  and the respective prior distributions. This latter term can be calculated analytically since both  $q(\widetilde{\mathbf{W}}_i)$  and  $p(\widetilde{\mathbf{W}}_i)$  are multivariate Gaussian distributions for  $i = 1, \dots, n$ .

The term  $\mathcal{E}_1$  cannot be evaluated analytically. However, since it is an expectation, it can be approximated using Monte Carlo:

$$\mathcal{E}_1 \approx \frac{1}{N_{MC}} \sum_{l=1}^{N_{MC}} \log p(\mathbf{Z} \mid \mathbf{F}_n^{(l)}, \boldsymbol{\tau}_{n+1}, \sigma_\epsilon^2),$$

where  $N_{MC}$  is the number of Monte Carlo samples used in the approximation and  $\mathbf{F}_n^{(l)} \sim q(\mathbf{F}_n \mid \underline{\Theta}_n)$ . Since the term  $\mathcal{E}_1$  is approximated through Monte Carlo, this type of variational inference is often referred to as stochastic variational inference.

A sample  $\mathbf{F}_n^{(l)}$  can be obtained easily by noting that  $q(\mathbf{F}_n \mid \underline{\Theta}_n)$  can be expressed as the marginalisation

$$\begin{aligned} q(\mathbf{F}_n \mid \underline{\Theta}_n) &= \int p(\mathbf{F}_n \mid \mathbf{F}_{n-1}, \widetilde{\mathbf{W}}_n, \underline{\Theta}_n) p(\mathbf{F}_{n-1} \mid \mathbf{F}_{n-2}, \widetilde{\mathbf{W}}_{n-1}, \underline{\Theta}_{n-1}) \cdots \\ &\quad \times p(\mathbf{F}_1 \mid \widetilde{\mathbf{W}}_1, \underline{\Theta}_1) q(\widetilde{\mathbf{W}}_n) \cdots q(\widetilde{\mathbf{W}}_1) d\mathbf{F}_{n-1} d\widetilde{\mathbf{W}}_n. \end{aligned} \quad (11)$$

In our case, the distributions  $p(\mathbf{F}_i \mid \mathbf{F}_{i-1}, \widetilde{\mathbf{W}}_i, \Theta_i), i = 1, \dots, n$ , are degenerate at  $\mathbf{F}_i = \mathbf{g}_i(\mathbf{W}_i \phi_i(\mathbf{F}_{i-1}; \Theta_i); \widetilde{\mathbf{F}}_{i-1})$ , where recall that  $\mathbf{W}_i \equiv h_i^{-1}(\widetilde{\mathbf{W}}_i), i = 1, \dots, n$ . Sampling thus proceeds by first sampling  $\widetilde{\mathbf{W}}_n^{(l)}$  from the variational distributions, back-transforming layer-wise to obtain  $\mathbf{W}_n^{(l)}$ , and then computing  $\mathbf{F}_n^{(l)}$  through

$$\mathbf{F}_n^{(l)} = \mathbf{g}_n(\mathbf{W}_n^{(l)} \phi_n(\mathbf{g}_{n-1}(\mathbf{W}_{n-1}^{(l)} \phi_{n-1}(\dots \mathbf{g}_1(\mathbf{W}_1^{(l)} \phi_1(\mathbf{S}; \Theta_1); \widetilde{\mathbf{S}}) \dots; \Theta_{n-1}); \widetilde{\mathbf{F}}_{n-2}^{(l)}); \Theta_n); \widetilde{\mathbf{F}}_{n-1}^{(l)}. \quad (12)$$

Equation (12) shows that all that is needed to sample  $\mathbf{F}_n$  is to (deterministically) propagate  $\mathbf{S}$  and  $\widetilde{\mathbf{S}}$  through the layers and rescaling functions with the weights fixed to the back-transformed sample  $\mathbf{W}_n^{(l)}$ .

Now, in variational Bayes one sets out to find the variational parameters (in our case the mean and Cholesky-factor elements) that maximise the lower bound, but these parameters no longer appear explicitly inside the partial objective  $\mathcal{E}_1$  due to the use of the Monte Carlo samples. However, since  $q(\widetilde{\mathbf{w}}_i^{(k)})$  is Gaussian, a sample from  $q(\widetilde{\mathbf{w}}_i^{(k)})$  is also a sample from  $\mathbf{m}_i^{(k)} + \mathbf{L}_i^{(k)}(\boldsymbol{\eta}_i^{(k)})\mathbf{e}_i^{(k)}$  where  $\mathbf{e}_i^{(k)} \sim \text{Gau}(\mathbf{0}, \mathbf{I})$ . This so-called re-parameterisation trick (Kingma and Welling, 2014; Xu et al., 2018) ensures that the set of variational parameters still explicitly appear within  $\mathcal{E}_1$  despite the use of a Monte Carlo approximation.

The optimisation problem reduces to the following. Let  $\mathbf{M}_i \equiv (\mathbf{m}_i^{(1)}, \dots, \mathbf{m}_i^{(d_i)})$  and  $\underline{\mathbf{M}}_n \equiv \{\mathbf{M}_1, \dots, \mathbf{M}_n\}$ . Similarly, let  $\boldsymbol{\Gamma}_i \equiv (\boldsymbol{\eta}_i^{(1)}, \dots, \boldsymbol{\eta}_i^{(d_i)})$  and  $\underline{\boldsymbol{\Gamma}}_n = \{\boldsymbol{\Gamma}_1, \dots, \boldsymbol{\Gamma}_n\}$ . Then

$$\begin{aligned} (\widehat{\underline{\mathbf{M}}}_n, \widehat{\underline{\boldsymbol{\Gamma}}}_n, \widehat{\underline{\Theta}}_n, \widehat{\boldsymbol{\tau}}_{n+1}, \widehat{\sigma}_\epsilon^2) = & \arg \max_{\underline{\mathbf{M}}_n, \underline{\boldsymbol{\Gamma}}_n, \underline{\Theta}_n, \boldsymbol{\tau}_{n+1}, \sigma_\epsilon^2} \frac{1}{N_{MC}} \sum_{l=1}^{N_{MC}} \log p(\mathbf{Z} \mid \mathbf{F}_n^{(l)}, \boldsymbol{\tau}_{n+1}, \sigma_\epsilon^2, ) \\ & - \sum_{i=1}^n KL(q(\widetilde{\mathbf{W}}_i) \parallel p(\widetilde{\mathbf{W}}_i)), \end{aligned} \quad (13)$$

where the dependence of  $\mathbf{F}_n^{(l)}$  on  $\underline{\mathbf{M}}_n, \underline{\boldsymbol{\Gamma}}_n$ , and  $\underline{\Theta}_n$  is given through (12) and application of the re-parameterisation trick to  $\widetilde{\mathbf{W}}_n$ .

## Prediction

The variational prediction distribution for  $\mathbf{Y}^*$  is given by

$$\begin{aligned} p(\mathbf{Y}^* \mid \mathbf{Z}, \widehat{\underline{\Theta}}_n, \widehat{\boldsymbol{\tau}}_{n+1}, \widehat{\sigma}_\epsilon^2) = & \int p(\mathbf{Y}^* \mid \mathbf{w}_{n+1}, \mathbf{F}_n^*) p(\mathbf{w}_{n+1} \mid \mathbf{F}_n, \mathbf{Z}, \widehat{\boldsymbol{\tau}}_{n+1}, \widehat{\sigma}_\epsilon^2) \\ & \times q(\mathbf{F}_n, \mathbf{F}_n^* \mid \widehat{\underline{\Theta}}_n) d\mathbf{w}_{n+1} d\mathbf{F}_n d\mathbf{F}_n^*, \end{aligned} \quad (14)$$

where  $q(\mathbf{F}_n, \mathbf{F}_n^* \mid \widehat{\underline{\Theta}}_n)$  is the (joint) variational posterior distribution over  $\mathbf{F}_n$  and  $\mathbf{F}_n^*$ . Samples from this joint distribution can be generated by noting that

$$\begin{aligned} q(\mathbf{F}_n, \mathbf{F}_n^* \mid \underline{\Theta}_n) = & \int p(\mathbf{F}_n^* \mid \mathbf{F}_{n-1}^*, \widetilde{\mathbf{F}}_{n-1}, \widetilde{\mathbf{W}}_n, \Theta_n) p(\mathbf{F}_n \mid \mathbf{F}_{n-1}, \widetilde{\mathbf{W}}_n, \Theta_n) \\ & \times p(\mathbf{F}_{n-1}^* \mid \mathbf{F}_{n-2}^*, \widetilde{\mathbf{F}}_{n-2}, \widetilde{\mathbf{W}}_{n-1}, \Theta_{n-1}) p(\mathbf{F}_{n-1} \mid \mathbf{F}_{n-2}, \widetilde{\mathbf{W}}_{n-1}, \Theta_{n-1}) \dots \\ & \times p(\mathbf{F}_1^* \mid \widetilde{\mathbf{W}}_1, \Theta_1) p(\mathbf{F}_1 \mid \widetilde{\mathbf{W}}_1, \Theta_1) q(\widetilde{\mathbf{W}}_n) \dots q(\widetilde{\mathbf{W}}_1) d\mathbf{F}_{n-1}^* d\mathbf{F}_{n-1} d\widetilde{\mathbf{W}}_n. \end{aligned}$$

Hence, as when fitting the model, one need only generate samples from  $q(\widetilde{\mathbf{W}}_n)$  and back-transform them layer-wise; these are then used to simultaneously generate samples (jointly) of  $\mathbf{F}_n$  and  $\mathbf{F}_n^*$ . Specifically, the warping  $\mathbf{F}_n^{(l)}$  is found from (12) and  $\mathbf{F}_n^{*(l)}$  is found from

$$\mathbf{F}_n^{*(l)} = \mathbf{g}_n(\mathbf{W}_n^{(l)} \phi_n(\mathbf{g}_{n-1}(\mathbf{W}_{n-1}^{(l)} \phi_{n-1}(\cdots \mathbf{g}_1(\mathbf{W}_1^{(l)} \phi_1(\mathbf{S}^*; \Theta_1); \widetilde{\mathbf{S}}) \cdots; \Theta_{n-1}); \widetilde{\mathbf{F}}_{n-2}^{(l)}; \Theta_n); \widetilde{\mathbf{F}}_{n-1}^{(l)}),$$

where  $\mathbf{S}^* = (\mathbf{s}_1, \dots, \mathbf{s}_{N^*})$  and recall that  $\widetilde{\mathbf{F}}_i^{(l)}$  is a submatrix of, or identical to,  $\mathbf{F}_i^{(l)}$ ,  $i = 1, \dots, n-1$ . Note that the samples of the transformed weights are obtained from the optimised variational distributions. That is, a sample from  $q(\widetilde{\mathbf{w}}_i^{(k)})$ , for  $i = 1, \dots, n$  and  $k = 1, \dots, d_i$ , is a sample from  $\text{Gau}(\widehat{\mathbf{m}}_i^{(k)}, \mathbf{V}_i^{(k)}(\widehat{\boldsymbol{\eta}}_i^{(k)}))$ , where  $\widehat{\mathbf{m}}_i^{(k)}$  and  $\widehat{\boldsymbol{\eta}}_i^{(k)}$  are obtained from (13). Therefore, for each sample of weights, the warped prediction locations and knots at each layer are found by simply (deterministically) propagating  $\mathbf{S}^*$  and  $\widetilde{\mathbf{S}}$  through the layers, respectively, with the weights fixed to the sample  $\underline{\mathbf{W}}_n^{(l)}$ .

The resulting approximation to (14) is the Gaussian mixture

$$p(\mathbf{Y}^* | \mathbf{Z}, \widehat{\Theta}_n, \widehat{\boldsymbol{\tau}}_{n+1}, \widehat{\sigma}_\epsilon^2) \approx \frac{1}{N_{MC}} \sum_{l=1}^{N_{MC}} \int p(\mathbf{Y}^* | \mathbf{w}_{n+1}, \mathbf{F}_n^{*(l)}) p(\mathbf{w}_{n+1} | \mathbf{F}_n^{(l)}, \mathbf{Z}, \widehat{\boldsymbol{\tau}}_{n+1}, \widehat{\sigma}_\epsilon^2) d\mathbf{w}_{n+1},$$

where each Gaussian mixture component has mean and covariance matrix defined through (6)–(9) with  $\mathbf{A}_{\widehat{\lambda}}$  replaced with  $\phi_{n+1}(\mathbf{F}_n^{(l)}; \Theta_{n+1})'$  and  $\mathbf{A}_{\widehat{\lambda}}^*$  replaced with  $\phi_{n+1}(\mathbf{F}_n^{*(l)}; \Theta_{n+1})'$ . Since each Gaussian distribution in the mixture has equal weighting, we suggest sampling a small amount of samples (say 100) from each component, and combining them to obtain an empirical approximation of  $p(\mathbf{Y}^* | \mathbf{Z}, \widehat{\Theta}_n, \widehat{\boldsymbol{\tau}}_{n+1}, \widehat{\sigma}_\epsilon^2)$ . In contrast to the SIWGP, note that these marginal prediction distributions can be highly non-Gaussian.

## 4 Experiments

We assessed the SIWGP and the SDSP on both simulated data and real data, and compared their predictive performance to those of various models. We consider two simple one-dimensional examples in Section 4.1, a two-dimensional example in Section 4.2, and images of cloud and ice taken from the MODIS instrument aboard the Aqua satellite in Section 4.3. In all cases, predictive performance was assessed by evaluating diagnostics on validation data, namely the mean absolute prediction error (MAPE), the root mean-squared-prediction-error (RMSPE), the continuous ranked probability score (CRPS), and the interval score at the 5% level (IS); see Gneiting and Raftery (2007). All experiments were carried out on a high-end desktop computer with 32GB of RAM, an Intel® Core™ i9-7900X CPU, and an NVIDIA® 1080 Ti GPU. Data and reproducible code for all experiments is provided in the Supplementary Material.

### 4.1 1D simulations

The first experiment assesses the suitability of the SIWGP and SDSP in modelling non-stationary processes, and compares them to other existing deep and shallow models, on

simple case studies. We consider two cases, where the underlying processes are

$$Y^{(1,1)}(s) = \begin{cases} -0.5 & |s| > 0.2 \\ 0.5 & \text{otherwise,} \end{cases} \quad Y^{(1,2)}(s) = \begin{cases} \exp\left(4 + \frac{5}{2s(10s+5)}\right) & -0.5 < s < 0 \\ 1 & 0.2 \leq s \leq 0.3 \\ -1 & 0.3 < s \leq 0.4 \\ 0 & \text{otherwise.} \end{cases} \quad (15)$$

The first process  $Y^{(1,1)}$  is a step function while the process  $Y^{(1,2)}$  is the same, up to a scaling of  $s$ , as that considered by Monterrubio-Gómez et al. (2018), and contains a smooth component and a discontinuous component. For both cases we used 300 spatial points randomly generated on  $[-0.5, 0.5]$  as our observation locations, and generated data at these 300 locations by adding Gaussian measurement error with zero mean and variance  $\sigma_\epsilon^2 = 0.01$  to the process values at these locations. We used a fine grid of 1001 points on the interval  $[-0.5, 0.5]$  as our prediction domain; this grid was used for computing the validation diagnostics outlined in the introduction to this section.

The SIWGP and SDSPs were configured to have an AWU as the hidden layer with 50 sigmoid functions regularly placed on  $[-0.5, 0.5]$  and  $\theta_{1j1} = 200$  in (4), for  $j = 1, \dots, 50$ . The second (output) layer was configured to have 50 bisquare functions regularly distributed on  $[-0.5, 0.5]$ . For the SDSP, the covariance matrix of the variational distribution,  $\mathbf{V}_1^{(1)}(\boldsymbol{\eta}_1^{(1)})$ , was constrained to be diagonal, and  $N_{MC}$  was fixed to 10. An Adam optimiser (Kingma and Ba, 2014) was used to optimise the process and variational parameters. In both experiments we proceeded in three stages: We first optimised the transformed weights  $\tilde{\mathbf{w}}_1^{(1)}$  (in case of the SIWGP) or the variational means  $\mathbf{m}_1^{(1)}$  (in case of the SDSP) using 100 gradient steps, then all the other parameters with  $\tilde{\mathbf{w}}_1^{(1)}$  or  $\mathbf{m}_1^{(1)}$  fixed for another 100 steps, and then all parameters simultaneously for a final 100 steps. Convergence of the likelihood (SIWGP) and variational lower bound (SDSP) was monitored for each case.

We used the generated data to compare the deep spatial models to the full-rank  $n = 1$  DGP (DGPfull) of Schmidt and O’Hagan (2003), the random Fourier Features DGP of Cutajar et al. (2017) with  $n = 2$  (DGPRFF), the sparse DGP of Damianou and Lawrence (2013) with one hidden layer (DGPsparse), and a (shallow) GP with a Matérn covariance function with smoothness parameter  $\nu = 3/2$ . The former three models were constructed from GPs with squared-exponential covariance functions. Details on the implementation of these alternative models are available in Appendix A in the Supplementary Material. To check the validity of the approximate variational inferences in this simple setting we also ran Markov chain Monte Carlo (MCMC) on the weights on the SDSP after fixing the parameters at the top layer at those estimated by VB,  $\hat{\boldsymbol{\tau}}_{n+1}$  (SDSP-MCMC). Table 1 summarises the models we compared to each other, the associated inference method, the software used, and the hardware used. Software packages used include TensorFlow (Allaire and Tang, 2018), PyTorch,<sup>1</sup> GPflow (Matthews et al., 2017), and Stan (Carpenter et al., 2017).

For both processes, the predictions, and 95% prediction intervals, as well as the data points used for simulation, are depicted in the panels of Figure 4. The stationarity assump-

<sup>1</sup><https://pytorch.org/>

Table 1: Inference Method, Software, and Hardware Used for the Models Considered in the 1D Simulation Experiments.

Model	Inference method	Software	Hardware
DGPfull	Elliptical slice sampling	Python	CPU
DGPRFF	Stochastic variational inference	Python and PyTorch	GPU
DGPsparse	Variational inference	R and TensorFlow	GPU
GP	Maximum likelihood	Python and TensorFlow	GPU
SDSP	Stochastic variational inference	R and TensorFlow	GPU
SDSP-MCMC	Hamiltonian Monte Carlo	R and Stan	CPU
SIWGP	Maximum likelihood	R and TensorFlow	GPU

Table 2: Diagnostic Results for  $Y^{(1,1)}$  and  $Y^{(1,2)}$ .

Model	$n$	$Y^{(1,1)}$				$Y^{(1,2)}$			
		MAPE	RMSPE	CRPS	IS	MAPE	RMSPE	CRPS	IS
DGPfull	1	0.0184	0.0474	0.0150	0.2413	0.0381	0.0892	0.0292	0.5155
DGPRFF	2	0.0093	0.0393	0.0080	0.0824	0.0337	0.0821	0.0252	0.3089
DGPsparse	1	0.0294	0.0566	0.0212	0.2050	0.0484	0.1108	0.0365	0.5650
GP	0	0.0381	0.0712	0.0296	0.5058	0.0516	0.0958	0.0395	0.6329
SDSP	1	0.0115	0.0320	0.0084	0.1013	0.0256	0.0664	0.0188	0.2231
SDSP-MCMC	1	0.0119	0.0324	0.0092	0.1083	0.0264	0.0660	0.0195	0.2307
SIWGP	1	0.0124	0.0323	0.0085	0.0954	0.0262	0.0689	0.0195	0.2607

tion of the Matérn GP does not hold for these processes, and thus the GP inadequately predicts signal variability in regions where there is not any, and step transitions that are too smooth. Although all deep variants considered here contain only one or two hidden processes, they are mostly able to adequately distinguish between signal ‘dead zones’ and regions of signal variability, although not all are able to capture the steep step transitions. Note that with the SIWGP and SDSP the prediction uncertainty increases at the step transitions; this is to be expected since in these regions the domain is ‘stretched out,’ resulting in relative local data paucity. Increased uncertainty in (relatively) poorly observed regions of high signal variability is an attractive feature of these deep models.

From Table 2 we see that the SIWGP and SDSP outperform the other models with  $n \in \{0, 1\}$ , both in terms of prediction and uncertainty quantification. The SDSP’s performance is comparable to that of the DGPRFF with  $n = 2$  hidden layers for the step function (we could not obtain good predictions with the DGPRFF for  $n = 1$ ). Interestingly, we do not see a notable difference between the SIWGP and the SDSP in this simple example (we do notice a difference in performance on the more complicated models considered in later sections). Reassuringly, SDSP-MCMC provided very similar results to the SDSP fitted using VB.

While it is difficult to generalise the computational demands of the various models

and inferential methods considered, it is worth noting that fitting and prediction with the SIWGP required only 4 s, while with the SDSP only 8 s. On the other hand it took over one hour to generate 10,000 samples using `Stan`, a few hours to obtain a good fit with the DGPRFF model, and a few days to obtain useful MCMC traces from an elliptical slice sampler on the DGPfull model. This considerable computational advantage of the spatial deep models is due to both the parsimonious representation of the bijective warpings and the approximate inference schemes used.

## 4.2 2D simulations

The second experiment assesses whether the fitting mechanisms we employ are able to recover the underlying warping function when data are generated from an SIWGP with known architecture. We simulate data in two dimensions from two underlying SIWGPs,  $Y^{(2,1)}$  and  $Y^{(2,2)}$ . The first SIWGP,  $Y^{(2,1)}$ , is constructed from an AWU of 50 units in each dimension, and an SR-RBF(1) unit (hence  $n = 11$ ), while the second SIWGP,  $Y^{(2,2)}$ , is constructed from an AWU of 50 units in each dimension, an SR-RBF(1) unit, and a Möbius transform ( $n = 12$ ). For both cases, the steepness parameters in the AWUs were set to  $\theta_{ij1} = 200, j = 1, \dots, 50, i = 1, 2$ . The warping functions associated with the two SIWGPs are shown in the top-left panels of Figures 5 and 6, respectively.

Both  $Y^{(2,1)}$  and  $Y^{(2,2)}$  were modelled using 400 bisquare basis functions,  $\sigma^2$  was set to 1 and  $l$  to 0.04. Two thousand points were then uniformly sampled from  $G \equiv [-0.5, 0.5]^2$  and used as observation locations. Gaussian measurement error with variance  $\sigma_\epsilon^2 = 0.01$  was then added to the process at these locations to yield two simulation data sets with which to fit an SIWGP and SDSP. The simulated processes are shown in the bottom-left panels of Figures 5 and 6, respectively.

We fitted both an SIWGP and an SDSP to  $Y^{(2,1)}$  and  $Y^{(2,2)}$ , with both constructed using an AWU, an SR-RBF(1) unit, and a Möbius transformation unit. We used the same optimisation strategy as in Section 4.1, but this time 400 steps in each stage were required to ensure convergence. Fitting and predicting with the SIWGP took around 1 minute, while the SDSP took around 4 minutes.

The variational posterior mean of the warping functions  $\mathbf{f}$  for both case studies are shown in the top-right panels of Figures 5 and 6, respectively. In both cases the estimated warpings are, up to a fixed rotation, remarkably similar. The predictions faithfully reproduce the true process, although this is somewhat expected from 2000 points in two dimensions. What is strikingly different from standard Gaussian-process regression (even when anisotropic covariance functions are used) is the prediction standard error map, where the uncertainty is high in areas of high process variability and where the uncertainty ‘contours’ follow those of the underlying process. Indeed, the deep spatial models thus seem to provide a better representation of the underlying data-generating process. We will also observe this when we analyse radiances from the MODIS instrument in Section 4.3.

In Table 3 we compare the SIWGP to the SDSP for both processes. (We do not compare to other models in this experiment since data are generated from a known SIWGP). Here we see that the SDSP performs similarly to the SIWGP overall, but outperforms it in terms of the interval score. We expect that capturing uncertainty in the hidden layers becomes

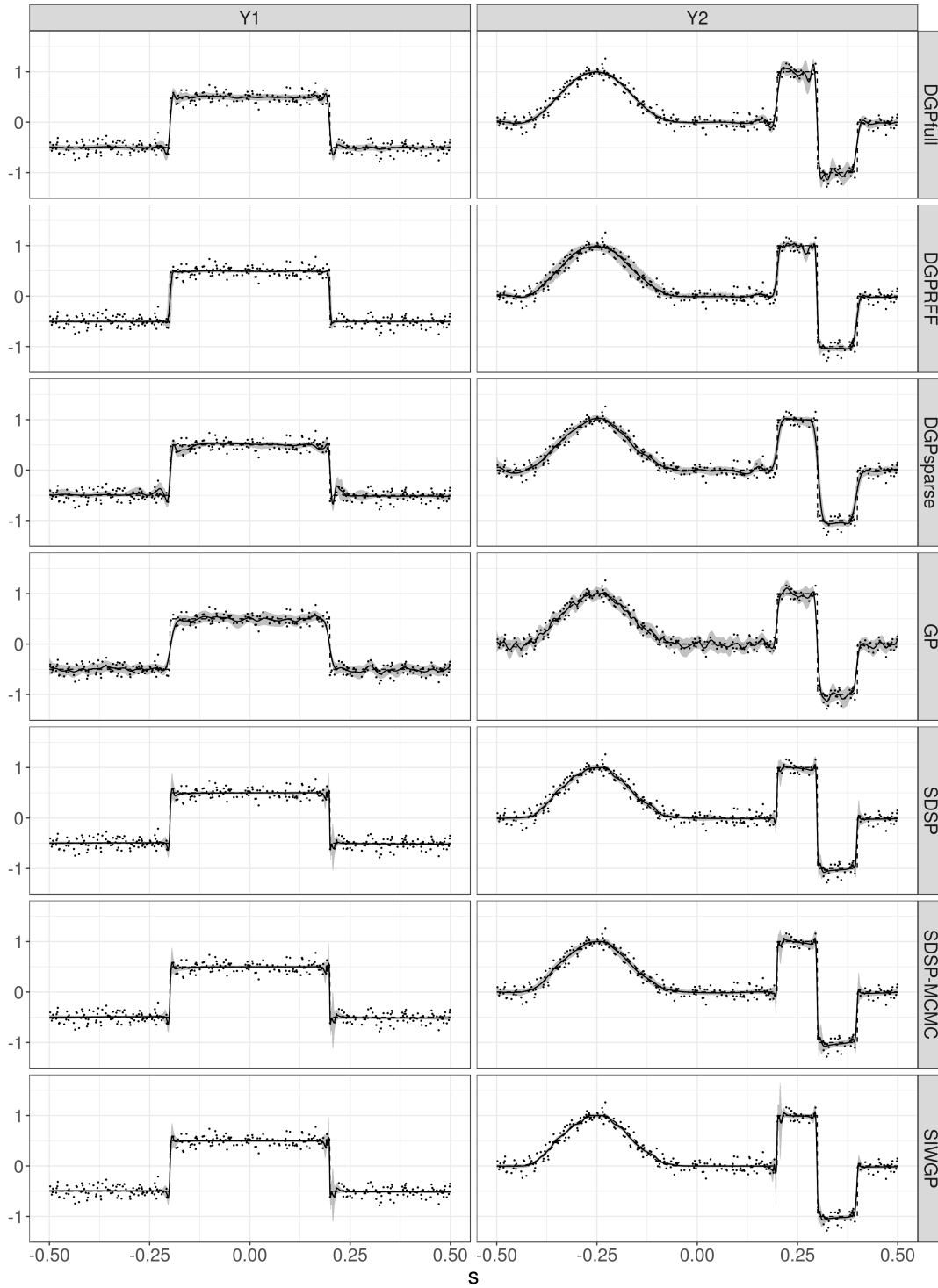


Figure 4: Data (dots), true process (dashed line), prediction (solid line) and 95% prediction interval (grey shading) for the two processes defined in (15) and the various models/inferential methods listed in Table 1.

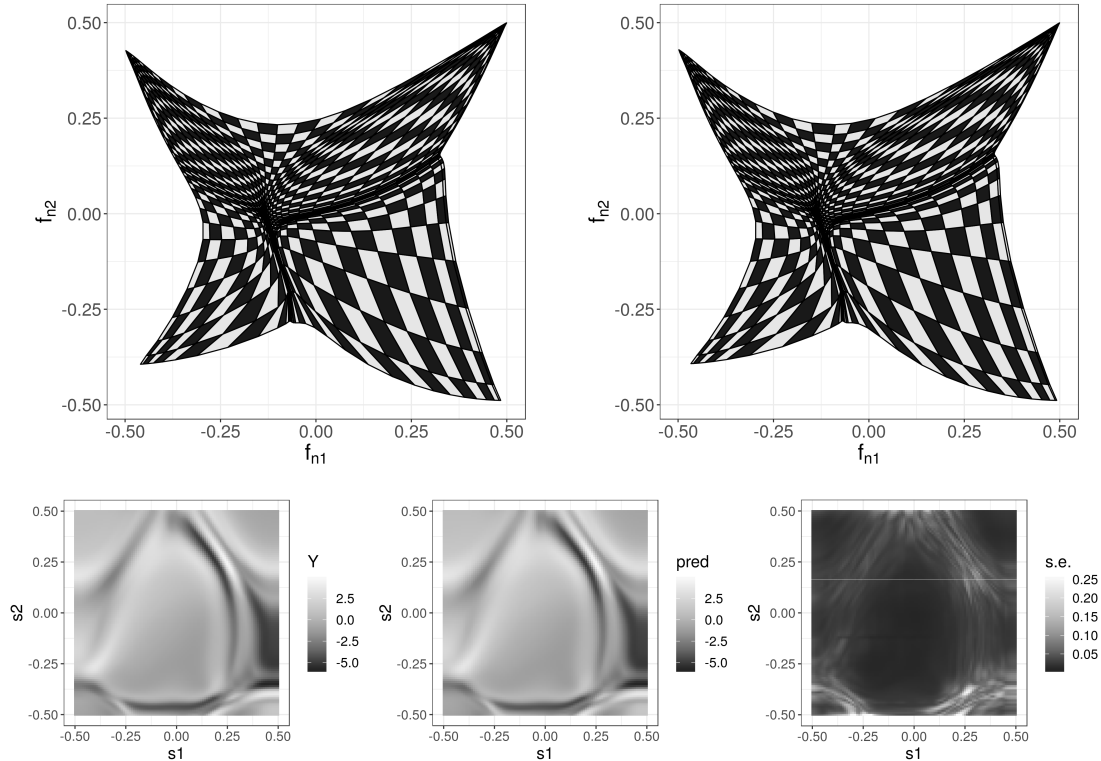


Figure 5: (Top-left) True warping function for the case  $Y^{(2,1)}$ , depicted here through its action on a regular chequered pattern on  $G$  and (top-right) its variational posterior mean following variational inference. (Bottom-left) the simulated process, (bottom-centre) the prediction and (bottom-right) the prediction standard error.

Table 3: Diagnostic Results for  $Y^{(2,1)}$  and  $Y^{(2,2)}$ .

Process	Model	MAPE	RMSPE	CRPS	IS
$Y^{(2,1)}$	SIWGP	0.0332	0.0498	0.0240	0.236
	SDSP	0.0333	0.0492	0.0236	0.208
$Y^{(2,2)}$	SIWGP	0.0609	0.0949	0.0462	0.633
	SDSP	0.0589	0.0885	0.0436	0.533

important for quantifying uncertainty in the output layer when the number of layers, and hence the number of hidden weights, increases.

### 4.3 Experiment using MODIS L1B radiances

The last experiment assesses the utility of the SDSP in applied settings. The experiment was constructed from spatial calibrated L1B radiances at a 500 m resolution obtained

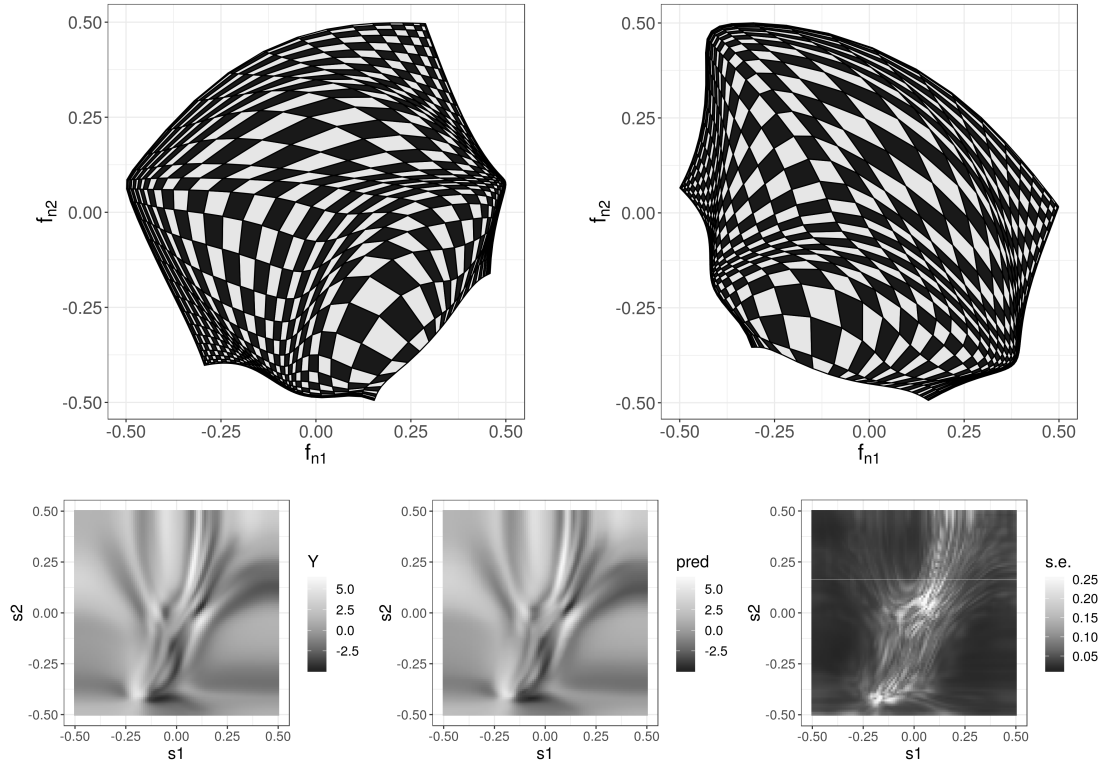


Figure 6: Same as Figure 5 but for the case  $Y^{(2,2)}$ .

from the Moderate Resolution Imaging Spectroradiometer (MODIS) instrument aboard the Aqua satellite (MODIS Characterization Support Team, 2015). In the product, radiances in units of  $W/m^2/\mu m/st$  are provided for 36 bands in the range  $0.4 \mu m$  to  $14.4 \mu m$  region of the electromagnetic spectrum. Here we considered the third of these bands, ranging from  $0.459 \mu m$  to  $0.479 \mu m$ , which is within the visible spectrum.

The L1B product is composed of several scenes that are of size  $2708 \times 4060$  pixels. Since these scenes are at a very high resolution we first regridded them into scenes of size  $136 \times 203$  that are at a 10 km resolution. From these we then sampled 4000 grid cells at random to make up our observed data set; the other 23,608 grid cells were left for out-of-sample validation. The goal was to assess the performance of the deep models in predicting these out-of-sample data from the 4000 ‘observed’ data.

In the course of our study we found that the DSPs perform as well as stationary Gaussian-process models when there is no clear nonstationarity, or only mild nonstationarity in the visible image. On the other hand, considerable improvement in predictive performance could be achieved when there was clear structured nonstationarity. In this section we present two scenes, shown in Figure 7, where we found that catering for a high degree of nonstationarity proved particularly beneficial. The first scene is from 04 December 2018 15:00 UTC over Antarctica, with radiances being detected from both ice and clouds. While radiances from the ice regime are almost spatially constant, those from the

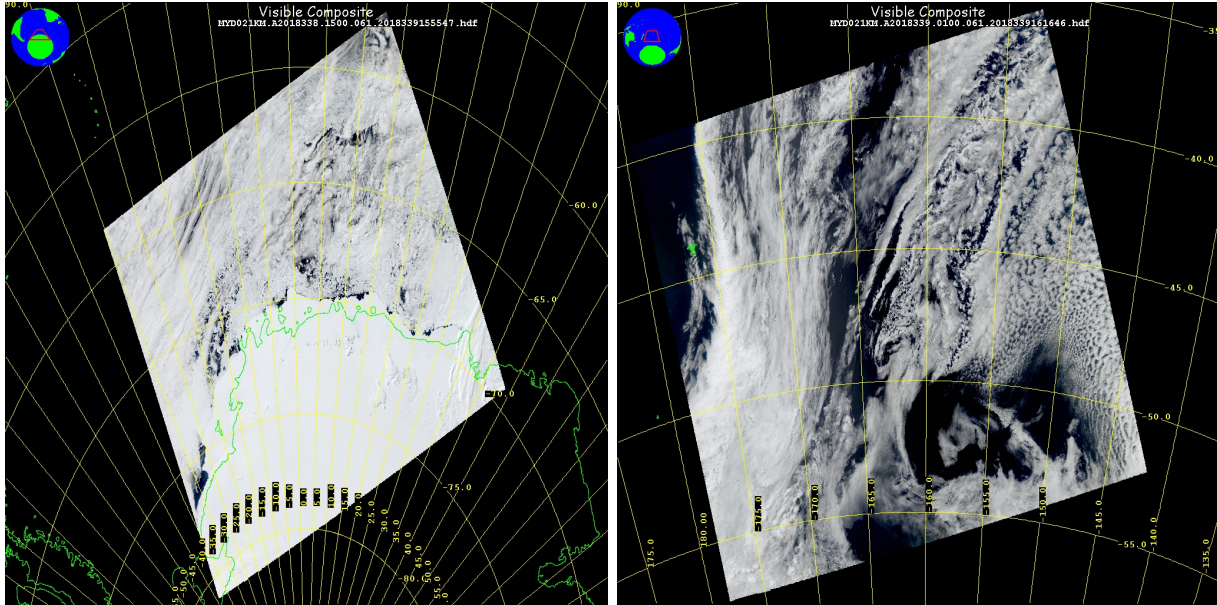


Figure 7: Calibrated L1B radiances in the  $0.459\ \mu\text{m}$  to  $0.479\ \mu\text{m}$  band from the MODIS instrument aboard the Aqua satellite. Longitudinal and latitudinal lines are shown in yellow while land boundaries are shown in green. The inset in the top-left corner of each image shows the location of the scene on the globe. The images were taken on 04 December 2018 15:00 UTC (left panel) and 05 December 2018 01:00 UTC (right panel), respectively. The images are courtesy of NASA (Source: <https://ladsweb.modaps.eosdis.nasa.gov>).

clouds are clearly more variable, and exhibit spatially-varying anisotropy. The second scene is from 05 December 2018 01:00 UTC in the South Pacific, just east of New Zealand. Here the radiances are predominantly from clouds that exhibit complex spatial nonstationarity.

For this study we considered an SDSP with two AWUs (one for each spatial dimension) composed of 50 sigmoid functions each, a multi-resolution RBF unit consisting of SR-RBF(1) and SR-RBF(2) units, and a Möbius transformation for a total of  $n = 93$  layers. We used  $r_{n+1} = 1600$  bisquare basis functions in the top layer. In the experiment we compared the SIWGP and SDSP to standard Gaussian process regression with a stationary, isotropic exponential covariance function, where the covariance function was fitted using standard variogram techniques. We also compared it to a shallower version of the SDSP containing only an SR-RBF(1) unit (SDSP-RBF) and an  $n = 0$  shallow model where  $r_1 = 1600$  bisquare basis functions. This latter  $n = 0$  model is identical to that considered by Zammit-Mangion and Cressie (2019), and we thus denote it as the ‘FRK’ (short for Fixed Rank Kriging) model. We employ the FRK model so that we can assess the benefit of including a warping function when the number of basis functions in the top layer is fixed by design (e.g., because of computational requirements).

In Figure 8 we show the full data set, the observations that were used for making inference, and the predictions and prediction standard errors from the SDSP and Gaussian process. The SDSP adapts to the different regimes of ice and cloud, providing an almost constant prediction over the ice coupled with very low prediction variance, and

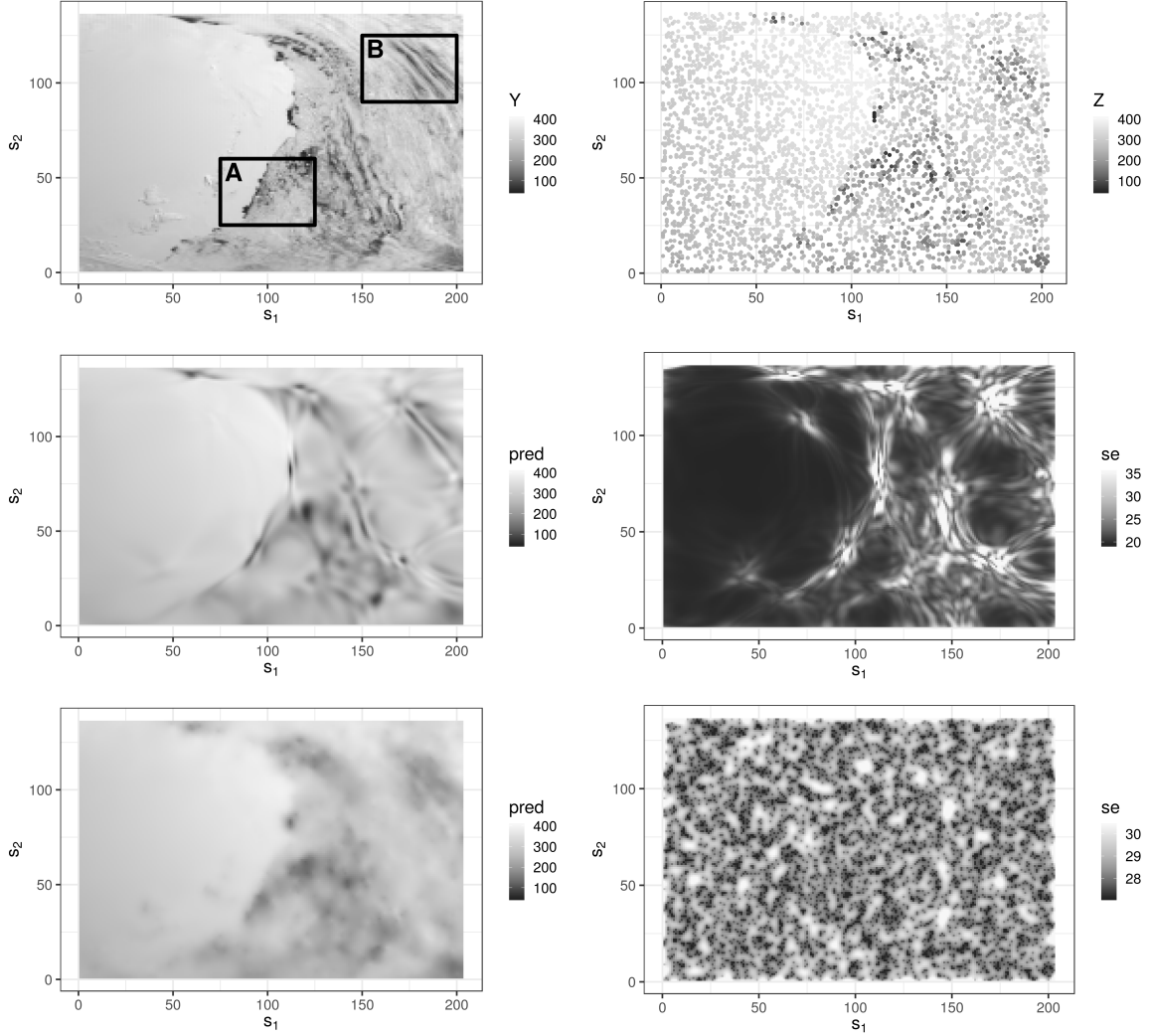


Figure 8: Results corresponding to the scene shown in the left panel of Figure 7. (Top-left) The scene regridded to a lower resolution, with black squares marking insets A and B shown in more detail in the top two rows of Figure 10. (Top-right) The observation data, sampled uniformly from the gridded data. (Centre) The prediction (left) and prediction standard error (right) when modelling using the SDSP. (Bottom) The prediction (left) and prediction standard error (right) when using Gaussian-process regression with stationary, isotropic exponential covariance function. All values shown are in units of  $W/m^2/\mu m/st$ .

spatially-varying isotropy over the region containing clouds. The inferred spatially-varying anisotropy is apparent in regions of high variability from the map of prediction standard errors. Gaussian process regression, as expected, smooths out most of the salient features that could be extracted from the data shown in the top-right panel. Furthermore, the prediction standard-error maps are reflective of the stationarity assumption, with no distinction made between the ice–cloud regimes. A similar conclusion can be made from

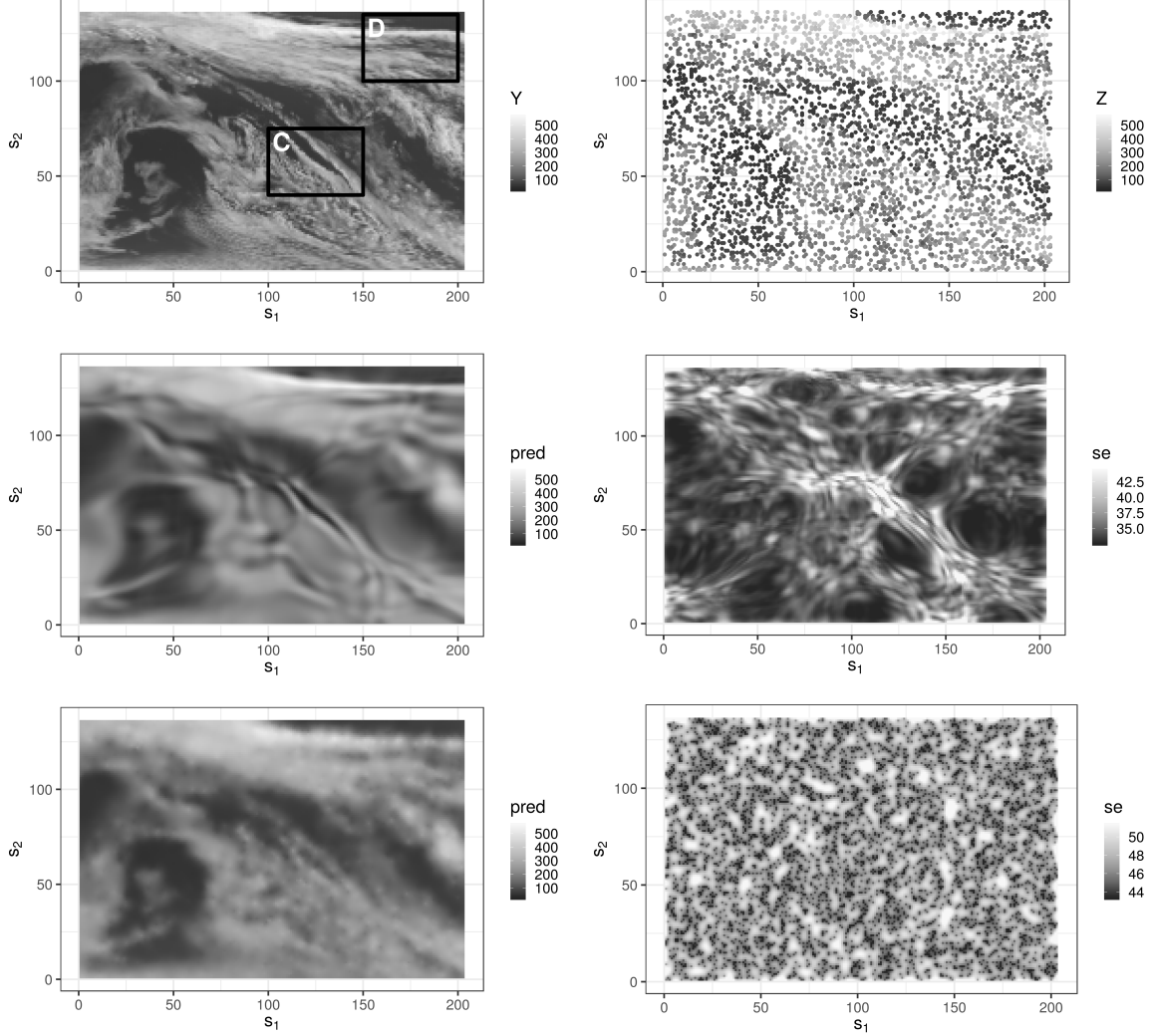


Figure 9: Results corresponding to the scene shown in the right panel of Figure 7. (Top-left) The scene regridded to a lower resolution, with black squares marking insets C and D shown in more detail in the bottom two rows of Figure 10. (Top-right) The observational data, sampled uniformly from the gridded data. (Centre) The prediction (left) and prediction standard error (right) when modelling using the SDSP. (Bottom) The prediction (left) and prediction standard error (right) when using Gaussian-process regression with stationary, isotropic exponential covariance function. All values shown are in units of  $W/m^2/\mu m/st$ .

Figure 9 where complex spatially-varying anisotropy predominant in this scene is correctly captured by the SDSP.

Diagnostics for the two scenes and the models we considered are shown in Table 4. We see that for these two scenes the improvement in prediction accuracy and uncertainty quantification over the other models, using the diagnostics we considered, is on the order of 5%. The improvement of the SDSP over the FRK model is more apparent, suggesting

Table 4: Diagnostic Results for the Two MODIS Scenes.

Scene	Model	MAPE	RMSPE	CRPS	IS
1	FRK	17.18	29.09	14.72	187.19
	GP	15.66	26.96	13.76	171.87
	SDSP	15.27	25.90	12.51	156.51
	SDSP-RBF	16.42	27.90	14.03	179.85
2	FRK	29.20	40.62	21.94	225.11
	GP	27.76	39.10	21.46	224.56
	SDSP	26.53	36.36	19.66	195.08
	SDSP-RBF	27.65	38.21	20.72	209.49

that the inclusion of the warping layer in several of the low-rank models used in spatial statistics may be especially beneficial.

Despite these improvements in the diagnostics we consider, the greater utility of the SDSP lies in its ability to predict spatial features that regular Gaussian-process models can not. We show such an example in Figure 10, which zooms into four regions, two from each scene (as marked in the top-left panels of Figure 8 and 9, respectively). In the top row we see some rocky outcrops delineating the land boundary of Antarctica correctly reproduced by the SDSP, while in the remaining rows, we see sharp boundaries in cloud cover being predicted.

One way to quantify the improvement in prediction is through a field comparison method (Wikle et al., 2019, Chapter 6) such as the threat score (TS, Wilks, 2006, Chapter 7) which, for a given binary classification of each pixel in an image, is defined as the number of true positives divided by the sum of true positives and incorrect classifications. The TS is bounded from above by one, and a higher TS constitutes a better prediction. We construct a binary version of our ‘true’ process by thresholding at  $Z_{\text{obs}}^{\text{th}} = 160 \text{ W/m}^2/\mu\text{m/st}$ ; anything below this threshold is deemed to not be cloud or ice and classified as a positive. We then take the predictions from each of our models, and threshold them using thresholds,  $Z_{\text{pred}}^{\text{th}}$ , ranging between 50 and 250  $\text{W/m}^2/\mu\text{m/st}$ . For each of the resulting binary predictions we then compute the TS with respect to the original thresholded image.

The resulting TSs for Insets A–D shown in Figure 10 are displayed in Figure 11. The highest TS is generally not obtained at  $Z_{\text{obs}}^{\text{th}}$ , however the SDSP gives considerably higher TSs for nearly all  $Z_{\text{pred}}^{\text{th}}$ . Of particular note is Inset B in the first scene, where the GP recorded a TS of 0 when  $Z_{\text{pred}}^{\text{th}} = Z_{\text{obs}}^{\text{th}}$ . This is a consequence of the GP oversmoothing the salient features in the data, a drawback which the SDSP, which is highly adaptive to such features, has the ability to remedy.

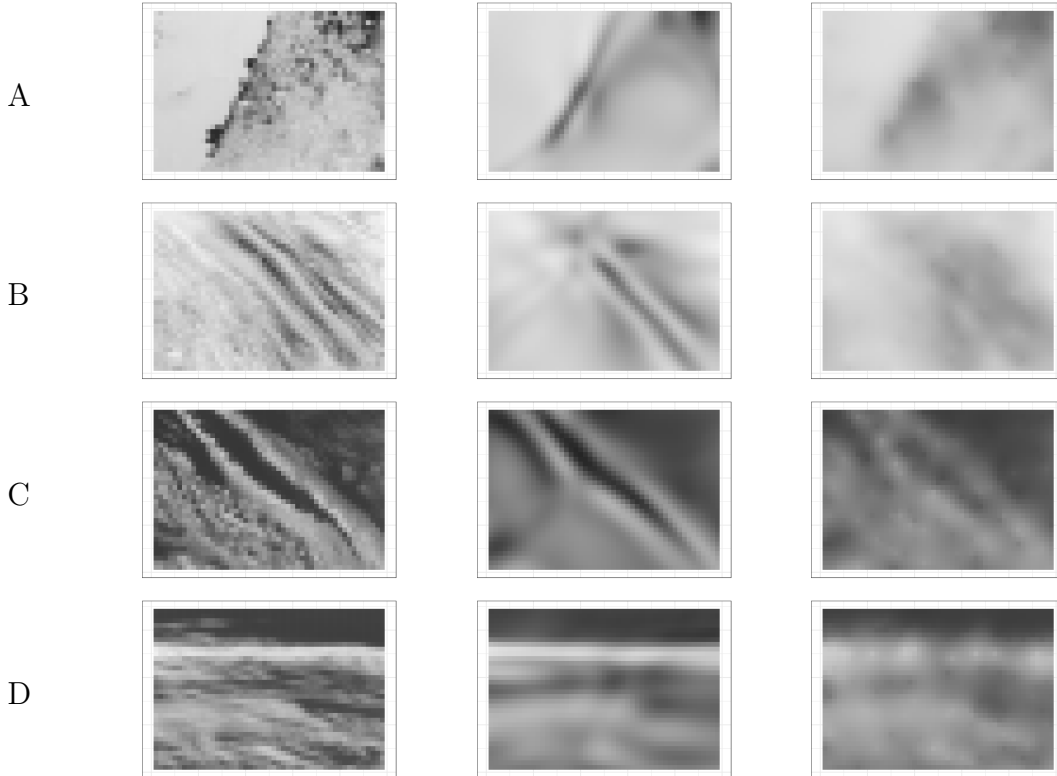


Figure 10: Insets corresponding to those marked in Figure 8 (top two rows) and in Figure 9 (bottom two rows), labelled A–D. The first column of images shows true values, the second column shows the prediction using the SDSP, and the third column the prediction using Gaussian process regression with stationary, isotropic, exponential covariance function.

## 5 Conclusion

SIWGP and SDSP are deep-learning models that are able to model highly-complex non-stationary, anisotropic spatial processes. The bijective constraint inherent in their construction restricts the class of warpings and avoids the notorious problem of ‘space-folding.’ Deep-learning software frameworks, such as **TensorFlow**, facilitate the inference procedure associated with these models. Results on both simulated and real data show the huge potential of these models in applications of geostatistics. As part of this work we have developed an **R** package, `deepspat` (see the Supplementary Material), that renders their implementation straightforward.

This article has presented SIWGP and SDSP that are relatively simple, and there are a number of avenues that could be explored next to render the models more widely applicable. First, the model in the output layer is currently based on a low-rank model, and the number of basis functions needs to be small (on the order of one or two thousand). Several studies (e.g., Heaton et al., 2019) show that, for large datasets, higher-rank models are required to obtain good prediction accuracy. Such models are available with the use of sparse precision or covariance matrices; however sparse linear algebraic operations on

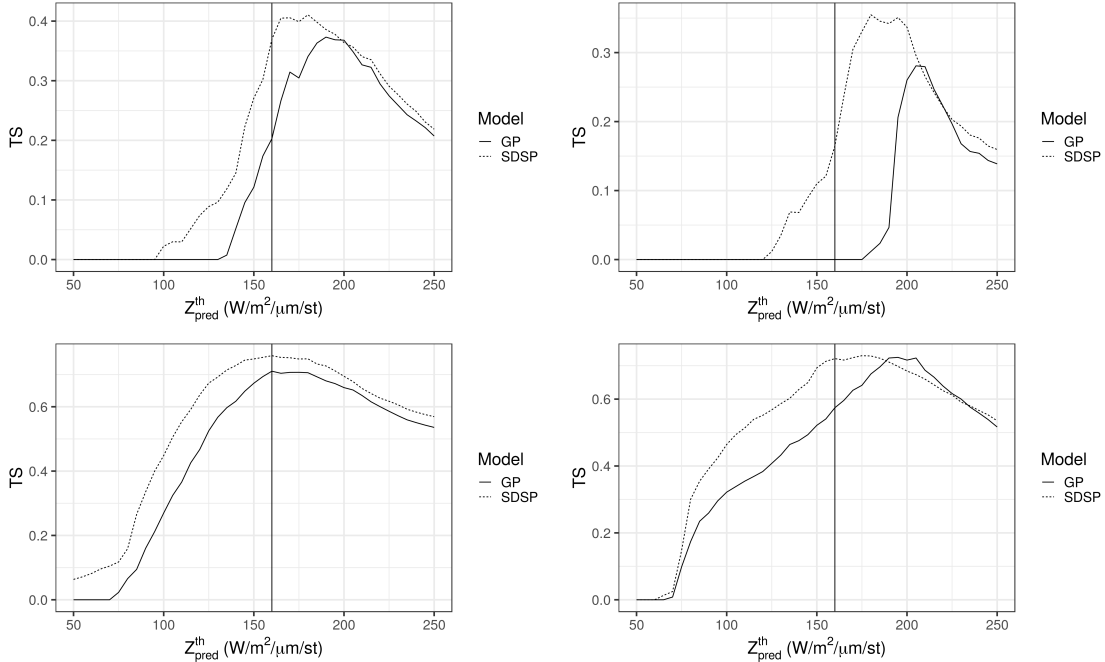


Figure 11: Threat scores as a function of threshold  $Z_{\text{pred}}^{\text{th}}$  when using the SDSP (dotted line) and the GP (solid line) for the insets A (top-left), B (top-right), C (bottom-left) and D (bottom-right) shown in Figure 10. The vertical lines denote the threshold used with the true values,  $Z_{\text{obs}}^{\text{th}} = 160 \text{ W/m}^2/\mu\text{m/st}$ .

GPUs tend to be considerably slower than their dense counterpart, and it is not clear at this stage whether such top-level models could be used within an SIWGP or SDSP. The use of a full-rank Gaussian process and composite-likelihood in the top layer (Eidsvik et al., 2014) is an attractive way forward for large datasets. Alternatively, one might explore the use of minibatch stochastic gradient descent for the SIWGP/SDSP; we give a brief description of how this could be done in Appendix B in the Supplementary Material.

Second, we have only considered some bijective warpings when constructing the deep architectures. Perrin and Monestiez (1999) considered other RBFs, while one can envisage others based on twists and spirals. A potentially useful unit not considered in this article is the *dimension-expansion* unit. As noted by Bornn et al. (2012), if  $\mathbf{f}(\mathbf{s}) = (s_1, s_2, \tilde{f}(\mathbf{s}))'$ , where  $\tilde{f}(\cdot)$  is some unknown map, then there is a trivial one-to-one mapping between  $\mathbf{s} = (s_1, s_2)'$  and  $\mathbf{f}(\mathbf{s})$ . New dimensions can be used to capture important features in the data, and can also be modelled using low-rank representations. Dimension expansion was recently used to warp space and time by Shand and Li (2017).

Third, we have kept the parameters in the AWUs and RBFs at each layer fixed. Inference might improve if some of these are also estimated; for example, in Section 4.1 we let  $\theta_{1j1} = 200$  for all  $j$ , while in Section 4.3 we found that  $\theta_{1j1} = 20$  for all  $j$ , gave more sensible warping functions. In higher-dimensional applications (for example spatio-temporal), covering the domain with RBFs would be challenging; a better strategy in this case might

be to use only a small set of RBFs and instead estimate their centroids and apertures. In the case of spatio-temporal data, using a parsimonious variant based on recurrent networks, as explored by McDermott and Wikle (2018), might be advantageous.

Fourth, we have not investigated the implication of the chosen *architectures* in our studies, that is, the choice of units and their ordering. Such considerations are important for our models – an axial warping followed by a Möbius transformation is very different from a Möbius transformation followed by an axial warping. The analyst has two options here, first to fit several models with different architectures and then either to use model averaging or model selection, or, second, to construct a very deep architecture containing several units repeatedly in a random order. Preliminary investigations of the latter case have shown that variational inference does not result in overfitting in these very deep networks, but that the benefit of this extra modelling effort was largely negligible (likely because of the relatively small datasets used).

Finally, in this article we have considered the SIWGP and SDSP in isolation of other process explanatory variables. We have also only considered Gaussian likelihood functions and point-referenced data. The applicability of the SIWGP/SDSP in these more challenging settings will be investigated in future work.

## Acknowledgements

Andrew Zammit-Mangion’s research was supported by an Australian Research Council (ARC) Discovery Early Career Research Award, DE180100203. Maurizio Filippone gratefully acknowledges support from the AXA Research Fund. The Aqua/MODIS Level 1B Calibrated Radiances (500m) data sets used in this work were acquired from the Level-1 and Atmosphere Archive & Distribution System (LAADS) Distributed Active Archive Center (DAAC), located in the Goddard Space Flight Center in Greenbelt, Maryland (<https://ladsweb.nascom.nasa.gov/>). The authors wish to thank Simone Rossi for running the code for the random Fourier features model and Matt Moores, Aidan Sims and Sébastien Marmin for helpful discussions.

## References

- Abadi, M., Agarwal, A., Barham, P., Brevdo, E., Chen, Z., Citro, C., Corrado, G. S., Davis, A., Dean, J., Devin, M., Ghemawat, S., Goodfellow, I., Harp, A., Irving, G., Isard, M., Jia, Y., Jozefowicz, R., Kaiser, L., Kudlur, M., Levenberg, J., Mané, D., Monga, R., Moore, S., Murray, D., Olah, C., Schuster, M., Shlens, J., Steiner, B., Sutskever, I., Talwar, K., Tucker, P., Vanhoucke, V., Vasudevan, V., Viégas, F., Vinyals, O., Warden, P., Wattenberg, M., Wicke, M., Yu, Y., and Zheng, X. (2015). TensorFlow: Large-scale machine learning on heterogeneous systems. *arXiv:1603.04467*.
- Allaire, J. J. and Tang, Y. (2018). *tensorflow: R Interface to ‘TensorFlow’*. Online: Available from <https://github.com/rstudio/tensorflow>.
- Anderes, E. B. and Stein, M. (2008). Estimating deformations of isotropic Gaussian random fields on the plane. *The Annals of Statistics*, 36:719–741.

- Arora, R., Basu, A., Mianjy, P., and Mukherjee, A. (2018). Understanding deep neural networks with rectified linear units. *arXiv:1611.01491*.
- Banerjee, S., Gelfand, A. E., Finley, A. O., and Sang, H. (2008). Gaussian predictive process models for large spatial data sets. *Journal of the Royal Statistical Society: Series B*, 70:825–848.
- Beal, M. J. (2003). *Variational Algorithms for Approximate Bayesian Inference*. PhD thesis, University of Cambridge, Cambridge, UK.
- Bengio, Y. and Delalleau, O. (2011). On the expressive power of deep architectures. In Kivinen, J., Szepesvári, C., Ukkonen, E., and Zeugmann, T., editors, *Proceedings of the 22nd International Conference on Algorithmic Learning Theory*, pages 18–36. Springer, New York, NY.
- Bishop, C. M. (2006). *Pattern Recognition and Machine Learning*. Springer-Verlag, Berlin, Germany.
- Blei, D. M., Kucukelbir, A., and McAuliffe, J. D. (2017). Variational inference: A review for statisticians. *Journal of the American Statistical Association*, 112:859–877.
- Bornn, L., Shaddick, G., and Zidek, J. V. (2012). Modeling nonstationary processes through dimension expansion. *Journal of the American Statistical Association*, 107:281–289.
- Bui, T., Hernández-Lobato, D., Hernandez-Lobato, J., Li, Y., and Turner, R. (2016). Deep Gaussian processes for regression using approximate expectation propagation. In Balcan, M. F. and Weinberger, K. Q., editors, *Proceedings of the 33rd International Conference on Machine Learning*, volume 48 of *Proceedings of Machine Learning Research*, pages 1472–1481. PMLR, New York, NY.
- Calandra, R., Peters, J., Rasmussen, C. E., and Deisenroth, M. P. (2016). Manifold Gaussian processes for regression. In *Proceedings of the 2016 International Joint Conference on Neural Networks (IJCNN)*, pages 3338–3345. IEEE, Vancouver, BC, Canada.
- Carpenter, B., Gelman, A., Hoffman, M. D., Lee, D., Goodrich, B., Betancourt, M., Brubaker, M., Guo, J., Li, P., and Riddell, A. (2017). Stan: A probabilistic programming language. *Journal of Statistical Software*, 76:1–32.
- Choi, T., Shi, J. Q., and Wang, B. (2011). A Gaussian process regression approach to a single-index model. *Journal of Nonparametric Statistics*, 23:21–36.
- Cressie, N. and Johannesson, G. (2008). Fixed rank kriging for very large spatial data sets. *Journal of the Royal Statistical Society: Series B*, 70:209–226.
- Cutajar, K., Bonilla, E. V., Michiardi, P., and Filippone, M. (2017). Random feature expansions for deep Gaussian processes. In Precup, D. and Teh, Y. W., editors, *Proceedings of the 34th International Conference on Machine Learning*, volume 70 of *Proceedings of Machine Learning Research*, pages 884–893. PMLR, Sydney, Australia.
- Dai, Z., Damianou, A., González, J., and Lawrence, N. (2016). Variational auto-encoded deep Gaussian processes. *arXiv:1511.06455*.
- Damian, D., Sampson, P. D., and Guttorp, P. (2001). Bayesian estimation of semi-parametric non-stationary spatial covariance structures. *Environmetrics*, 12:161–178.
- Damianou, A. and Lawrence, N. (2013). Deep Gaussian processes. In Carvalho, C. M. and Ravikumar, P., editors, *Proceedings of the Sixteenth International Conference on Artificial Intelligence and Statistics*, volume 31 of *Proceedings of Machine Learning Research*, pages 207–215, PMLR, Scottsdale, AZ.

- Dubrovin, B. A., Fomenko, A. T., and Novikov, S. P. (1992). *Modern Geometry – Methods and Applications. Part I*. Springer, New York, NY, 2nd edition.
- Dunlop, M. M., Girolami, M., Stuart, A. M., and Teckentrup, A. L. (2018). How deep are deep Gaussian processes? *Journal of Machine Learning Research*, 19:1–46.
- Duvenaud, D., Rippel, O., Adams, R., and Ghahramani, Z. (2014). Avoiding pathologies in very deep networks. In Kaski, S. and Corander, J., editors, *Proceedings of the Seventeenth International Conference on Artificial Intelligence and Statistics*, volume 33 of *Proceedings of Machine Learning Research*, pages 202–210, PMLR, Reykjavik, Iceland.
- Eidsvik, J., Shaby, B. A., Reich, B. J., Wheeler, M., and Niemi, J. (2014). Estimation and prediction in spatial models with block composite likelihoods. *Journal of Computational and Graphical Statistics*, 23:295–315.
- Eldan, R. and Shamir, O. (2016). The power of depth for feedforward neural networks. In Feldman, V., Rakhlin, A., and Shamir, O., editors, *29th Annual Conference on Learning Theory*, volume 49 of *Proceedings of Machine Learning Research*, pages 907–940, PMLR, New York, NY.
- Fouedjio, F., Desassis, N., and Romary, T. (2015). Estimation of space deformation model for non-stationary random functions. *Spatial Statistics*, 13:45–61.
- Fuglstad, G.-A., Simpson, D., Lindgren, F., and Rue, H. (2015). Does non-stationary spatial data always require non-stationary random fields? *Spatial Statistics*, 14:505–531.
- Gibbs, M. N. (1998). *Bayesian Gaussian processes for Regression and Classification*. PhD thesis, University of Cambridge, Cambridge, UK.
- Gneiting, T. and Raftery, A. E. (2007). Strictly proper scoring rules, prediction, and estimation. *Journal of the American Statistical Association*, 102:359–378.
- Goodfellow, I., Bengio, Y., Courville, A., and Bengio, Y. (2016). *Deep Learning*. MIT Press, Cambridge, MA.
- Heaton, M. J., Datta, A., Finley, A., Furrer, R., Guhaniyogi, R., Gerber, F., Gramacy, R. B., Hammerling, D., Katzfuss, M., Lindgren, F., et al. (2019). Methods for analyzing large spatial data: A review and comparison. *Journal of Agricultural, Biological, and Environmental Statistics*, in press.
- Hensman, J., Durrande, N., and Solin, A. (2017). Variational Fourier features for Gaussian processes. *Journal of Machine Learning Research*, 18:5537–5588.
- Hensman, J. and Lawrence, N. D. (2014). Nested variational compression in deep Gaussian processes. *arXiv:1412.1370*.
- Higdon, D., Swall, J., and Kern, J. (1999). Non-stationary spatial modeling. *Bayesian Statistics*, 6:761–768.
- Iovleff, S. and Perrin, O. (2004). Estimating a nonstationary spatial structure using simulated annealing. *Journal of Computational and Graphical Statistics*, 13:90–105.
- Kingma, D. P. and Ba, J. (2014). Adam: A method for stochastic optimization. *arXiv:1412.6980*.
- Kingma, D. P. and Welling, M. (2014). Auto-encoding variational Bayes. *arXiv:1312.6114*.
- Kleiber, W. (2016). High resolution simulation of nonstationary Gaussian random fields. *Computational Statistics & Data Analysis*, 101:277–288.
- Lange, M., Zühlke, D., Holz, O., and Villmann, T. (2014). Applications of  $l_p$ -norms and their smooth approximations for gradient based learning vector quantiza-

- tion. In *Proceedings of the 22nd European Symposium on Artificial Neural Networks*, Bruges, Belgium. Available from <https://www.elen.ucl.ac.be/esann/proceedings/electronicproceedings.htm>.
- Lázaro-Gredilla, M., Quiñonero-Candela, J., Rasmussen, C. E., and Figueiras-Vidal, A. R. (2010). Sparse spectrum Gaussian process regression. *Journal of Machine Learning Research*, 11:1865–1881.
- LeCun, Y., Bengio, Y., and Hinton, G. (2015). Deep learning. *Nature*, 521:436–444.
- Liang, S. and Srikant, R. (2017). Why deep neural networks for function approximation? *arXiv:1610.04161*.
- Lindgren, F., Rue, H., and Lindström, J. (2011). An explicit link between Gaussian fields and Gaussian Markov random fields: the stochastic partial differential equation approach. *Journal of the Royal Statistical Society: Series B*, 73:423–498.
- Marmin, S., Ginsbourger, D., Baccou, J., and Liandrat, J. (2018). Warped Gaussian processes and derivative-based sequential designs for functions with heterogeneous variations. *SIAM/ASA Journal on Uncertainty Quantification*, 6:991–1018.
- Matthews, D. G., Alexander, G., Van Der Wilk, M., Nickson, T., Fujii, K., Boukouvalas, A., León-Villagrà, P., Ghahramani, Z., and Hensman, J. (2017). GPflow: A Gaussian process library using TensorFlow. *Journal of Machine Learning Research*, 18:1299–1304.
- McDermott, P. L. and Wikle, C. K. (2018). Deep echo state networks with uncertainty quantification for spatio-temporal forecasting. *Environmetrics*, in press.
- Meiring, W., Monestiez, P., Sampson, P., and Guttorp, P. (1997). Developments in the modelling of nonstationary spatial covariance structure from space-time monitoring data. In Baa, E. Y. and Schofield, N., editors, *Geostatistics Wollongong '96*, pages 162–173. Kluwer, Dordrecht, The Netherlands.
- MODIS Characterization Support Team (2015). MODIS 500m Calibrated Radiance Product. NASA MODIS Adaptive Processing System, Goddard Space Flight Center, USA.
- Monestiez, P., Sampson, P. D., and Guttorp, P. (1993). Modelling of heterogeneous spatial correlation structure by spatial deformation. *Cahiers de Géostatistique*, 3:35–46.
- Monterrubio-Gómez, K., Roininen, L., Wade, S., Damoulas, T., and Girolami, M. (2018). Posterior inference for sparse hierarchical non-stationary models. *arXiv:1804.01431*.
- Morales, F. E. C., Gamerman, D., and Paez, M. S. (2013). State space models with spatial deformation. *Environmental and Ecological Statistics*, 20:191–214.
- Neal, R. M. (1996). *Bayesian Learning for Neural Networks*. Springer, New York, NY.
- Nychka, D., Bandyopadhyay, S., Hammerling, D., Lindgren, F., and Sain, S. (2015). A multiresolution Gaussian process model for the analysis of large spatial datasets. *Journal of Computational and Graphical Statistics*, 24:579–599.
- Paciorek, C. J. and Schervish, M. J. (2006). Spatial modelling using a new class of nonstationary covariance functions. *Environmetrics*, 17:483–506.
- Perrin, O. and Meiring, W. (1999). Identifiability for non-stationary spatial structure. *Journal of Applied Probability*, 36:1244–1250.
- Perrin, O. and Monestiez, P. (1999). Modelling of non-stationary spatial structure using parametric radial basis deformations. In Gómez-Hernández, J., Soares, A., and Froidevaux, R., editors, *GeoENV II—Geostatistics for Environmental Applications*, pages 175–186. Springer, New York, NY.

- Perrin, O. and Senoussi, R. (2000). Reducing non-stationary random fields to stationarity and isotropy using a space deformation. *Statistics & Probability Letters*, 48:23–32.
- Quiñonero-Candela, J. and Rasmussen, C. E. (2005). A unifying view of sparse approximate Gaussian process regression. *Journal of Machine Learning Research*, 6:1939–1959.
- R Core Team (2018). *R: A Language and Environment for Statistical Computing*. R Foundation for Statistical Computing, Vienna, Austria.
- Rasmussen, C. E. and Williams, C. K. (2006). *Gaussian Processes for Machine Learning*. The MIT Press, Cambridge, MA.
- Safran, I. and Shamir, O. (2017). Depth-width tradeoffs in approximating natural functions with neural networks. In Precup, D. and Teh, Y. W., editors, *Proceedings of the 34th International Conference on Machine Learning*, volume 70 of *Proceedings of Machine Learning Research*, pages 2979–2987. PMLR, Sydney, Australia.
- Salimbeni, H. and Deisenroth, M. (2017). Doubly stochastic variational inference for deep Gaussian processes. In Guyon, I., Luxburg, U., Bengio, S., Wallach, H., Fergus, R., Vishwanathan, S., and Garnett, R., editors, *Advances in Neural Information Processing Systems 30*, pages 4588–4599.
- Sampson, P., Damian, D., and Guttorp, P. (2001). Advances in modeling and inference for environmental processes with nonstationary spatial covariance. In Monestiez, P., Allard, D., and Froidevaux, R., editors, *GeoENV III—Geostatistics for Environmental Applications*, pages 17–32. Springer, New York, NY.
- Sampson, P. D. and Guttorp, P. (1992). Nonparametric estimation of nonstationary spatial covariance structure. *Journal of the American Statistical Association*, 87:108–119.
- Schmidt, A. M., Guttorp, P., and O’Hagan, A. (2011). Considering covariates in the covariance structure of spatial processes. *Environmetrics*, 22:487–500.
- Schmidt, A. M. and O’Hagan, A. (2003). Bayesian inference for non-stationary spatial covariance structure via spatial deformations. *Journal of the Royal Statistical Society: Series B*, 65:743–758.
- Shand, L. and Li, B. (2017). Modeling nonstationarity in space and time. *Biometrics*, 73:759–768.
- Smith, R. L. (1996). Estimating nonstationary spatial correlations. Online: Available from <http://citeseerx.ist.psu.edu/viewdoc/download?doi=10.1.1.40.5988&rep=rep1&type=pdf>.
- Snoek, J., Swersky, K., Zemel, R., and Adams, R. (2014). Input warping for bayesian optimization of non-stationary functions. In Xing, E. P. and Jebara, T., editors, *Proceedings of the 31st International Conference on Machine Learning*, volume 32 of *Proceedings of Machine Learning Research*, pages 1674–1682, PMLR, Beijing, China.
- Tan, L. S. and Nott, D. J. (2018). Gaussian variational approximation with sparse precision matrices. *Statistics and Computing*, 28:259–275.
- Titsias, M. and Lawrence, N. D. (2010). Bayesian gaussian process latent variable model. In Teh, Y. W. and Titterton, M., editors, *Proceedings of the Thirteenth International Conference on Artificial Intelligence and Statistics*, volume 9 of *Proceedings of Machine Learning Research*, pages 844–851, PMLR, Sardinia, Italy.
- Wikle, C. K., Zammit-Mangion, A., and Cressie, N. (2019). *Spatio-Temporal Statistics with R*. Chapman & Hall/CRC, Boca Raton, FL.

- Wilks, D. S. (2006). *Statistical Methods in the Atmospheric Sciences*. Academic Press, San Diego, MA, 2nd edition.
- Wilson, A. G., Hu, Z., Salakhutdinov, R., and Xing, E. P. (2016). Deep kernel learning. In Gretton, A. and Robert, C. C., editors, *Proceedings of the 19th International Conference on Artificial Intelligence and Statistics*, volume 51 of *Proceedings of Machine Learning Research*, pages 370–378, PMLR, Cadiz, Spain.
- Xiong, Y., Chen, W., Apley, D., and Ding, X. (2007). A non-stationary covariance-based kriging method for metamodelling in engineering design. *International Journal for Numerical Methods in Engineering*, 71:733–756.
- Xu, M., Quiroz, M., Kohn, R., and Sisson, S. A. (2018). Variance reduction properties of the reparameterization tricks. *arxiv:1809.10330*.
- Zammit-Mangion, A. and Cressie, N. (2019). FRK: An R package for spatial and spatio-temporal prediction with large datasets. *Journal of Statistical Software*, in press.
- Zidek, J. V., Sun, W., and Le, N. D. (2000). Designing and integrating composite networks for monitoring multivariate Gaussian pollution fields. *Journal of the Royal Statistical Society: Series C*, 49:63–79.

# A Details on the 1D Simulation Experiment

In this appendix we provide implementation details of the models we compared the SDSP/SIWGP to in Section 4.1. Details for DGPfull are presented in Section A.1; DGPRFF in Section A.2; DGPsparse in Section A.3; GP in Section A.4; and SDSP-MCMC in Section A.5. Note that in this appendix the notation differs slightly from that of the main text when describing the various methods; terms are explicitly defined, where appropriate, for the reader’s benefit.

## A.1 DGPfull

The DGPfull model we implemented is the following two-layer (i.e., one hidden layer) Gaussian process. Specifically, let  $\mathbf{Z} \equiv (Z_1, \dots, Z_N)'$  denote the data;  $\mathbf{Y} \equiv (Y_1, \dots, Y_N)'$  the process at the data locations  $\mathbf{S} \equiv (s_1, \dots, s_N)'$ ; and  $\mathbf{F}_1 = (f_{11}, \dots, f_{1N})'$  the warped locations. We let

$$\begin{aligned} \mathbf{Z} \mid \mathbf{Y} &\sim \text{Gau}(\mathbf{Y}, \sigma_\epsilon^2 \mathbf{I}), \\ \mathbf{Y} \mid \mathbf{F}_1 &\sim \text{Gau}(\mathbf{0}, \mathbf{K}_2(\mathbf{F}_1)), \\ \mathbf{F}_1 &\sim \text{Gau}(\mathbf{0}, \mathbf{K}_1(\mathbf{S})), \end{aligned}$$

where

$$\mathbf{K}_2(\mathbf{F}_1) \equiv (\sigma_2^2 \exp(-(f_{1i} - f_{1j})^2/\alpha_2) : i, j = 1, \dots, N), \quad (\text{A.1})$$

$$\mathbf{K}_1(\mathbf{S}) \equiv (\sigma_1^2 \exp(-(s_i - s_j)^2/\alpha_1) : i, j = 1, \dots, N), \quad (\text{A.2})$$

are covariance matrices constructed using the squared-exponential covariance function. Since estimating parameters in the DGPfull model is difficult, the parameters  $\sigma_\epsilon^2$ ,  $\sigma_i^2$ , and  $\alpha_i$ , for  $i = 1, 2$ , were estimated by fitting a DGPRFF model with squared-exponential covariance functions and one hidden layer. Specifically, for the first case study we fixed  $\log \sigma_\epsilon^2 = -4.336$ ,  $\log \sigma_1^2 = 0.713$ ,  $\log \sigma_2^2 = -0.067$ ,  $\log \alpha_1 = -2.194$ , and  $\log \alpha_2 = -1.406$ , while for the second case study we fixed  $\log \sigma_\epsilon^2 = -3.830$ ,  $\log \sigma_1^2 = 0.270$ ,  $\log \sigma_2^2 = 1.408$ ,  $\log \alpha_1 = -1.645$ , and  $\log \alpha_2 = -1.032$ .

Let  $\mathbf{Y}^* \equiv (Y_1^*, \dots, Y_{N^*}^*)'$  and  $\mathbf{F}_1^* \equiv (f_{11}^*, \dots, f_{1N^*}^*)'$  denote the processes and hidden layer variables at the  $N^*$  prediction locations. The conditional distribution of  $\mathbf{Y}$ , and hence of  $\mathbf{Y}^*$ , when conditioned on the data  $\mathbf{Z}$ , is not available in closed form, and was hence approximated using a Gibbs sampling Markov chain Monte Carlo (MCMC) scheme. Specifically, we iteratively sampled from the distributions  $p(\mathbf{Y} \mid \mathbf{F}_1, \mathbf{Z})$  and  $p(\mathbf{F}_1 \mid \mathbf{Y})$ . While the former of these is Gaussian and hence easy to sample from, the latter is not. As in Cutajar et al. (2017) we used elliptical slice sampling to sample from this conditional distribution. The full conditional distributions of  $\mathbf{Y}^*$  and  $\mathbf{F}_1^*$ , namely  $p(\mathbf{Y}^* \mid \mathbf{Y}, \mathbf{F}_1^*)$  and  $p(\mathbf{F}_1^* \mid \mathbf{F}_1)$ , are Gaussian and available in closed form. Thus, sampling from these distributions proceeds through sampling by composition: First samples of  $\mathbf{F}_1^* \mid \mathbf{F}_1$  are generated followed by samples of  $\mathbf{Y}^* \mid \mathbf{Y}, \mathbf{F}_1^*$ .

The MCMC scheme was implemented in `Python`. The number of iterations and burn-in samples were set to 5000 and 100, respectively. The elliptical slice sampler took, on

average, about 85 s to generate a single sample from the conditional distribution  $p(\mathbf{F}_1 | \mathbf{Y})$ . Convergence was assessed by visually inspecting trace plots of  $\mathbf{Y}^*$  at a small number of randomly-selected prediction locations.

## A.2 DGPRFF

We fit DGPRFF models with one, two, and five hidden layers. Of these, the model with two hidden layers provided the best predictive performance and, therefore, this is the model presented in the main text.

The DGPRFF model with two hidden layers (and a single-dimensional output at each layer) is the hierarchical model given by

$$\begin{aligned}\mathbf{Z} | \mathbf{Y} &\sim \text{Gau}(\mathbf{Y}, \sigma_\epsilon^2 \mathbf{I}), \\ \mathbf{Y} | \mathbf{F}_2 &\sim \text{Gau}(\mathbf{0}, \mathbf{K}_3(\mathbf{F}_2)), \\ \mathbf{F}_2 | \mathbf{F}_1 &\sim \text{Gau}(\mathbf{0}, \mathbf{K}_2(\mathbf{F}_1)), \\ \mathbf{F}_1 &\sim \text{Gau}(\mathbf{0}, \mathbf{K}_1(\mathbf{S})),\end{aligned}$$

where  $\mathbf{K}_3$ ,  $\mathbf{K}_2$ , and  $\mathbf{K}_1$  are constructed from squared-exponential covariance functions (see Section A.1). By Bochner’s Theorem, one can represent the squared-exponential correlation function as an expectation of sums and products of trigonometric functions, where the expectation is taken with respect to a Gaussian distribution (in the spectral domain) that is fully determined by the length scale parameter  $\alpha$ . One can therefore approximate this expectation (and, hence, the correlation function) through Monte Carlo to obtain a set of trigonometric basis functions that can be used to reconstruct the squared-exponential function in expectation; see Cutajar et al. (2017) for details.

In summary, dimension-reduction in the DGPRFF is achieved by modelling  $\mathbf{K}_i(\mathbf{F}_{i-1}) = \Phi_i(\mathbf{F}_{i-1}; \Theta_i) \Phi_i(\mathbf{F}_{i-1}; \Theta_i)'$ , for  $i = 1, 2, 3$ , and for  $\mathbf{S} \equiv \mathbf{F}_0$ , where  $\Phi_i$  are sine and cosine functions evaluated at the data/warped data locations. The ensuing weight-space view of the DGPRFF model is

$$\begin{aligned}\mathbf{Z} &= \mathbf{Y} + \boldsymbol{\varepsilon}, \\ \mathbf{Y} &= \Phi_3(\mathbf{F}_2; \Theta_3) \mathbf{w}_3, \\ \mathbf{F}_2 &= \Phi_2(\mathbf{F}_1; \Theta_2) \mathbf{w}_2, \\ \mathbf{F}_1 &= \Phi_1(\mathbf{S}; \Theta_1) \mathbf{w}_1,\end{aligned}$$

where  $\mathbf{w}_i \sim \text{Gau}(\mathbf{0}, \mathbf{I})$ ,  $i = 1, 2, 3$ , and  $\boldsymbol{\varepsilon} \sim \text{Gau}(\mathbf{0}, \sigma_\epsilon^2 \mathbf{I})$ . The parameters vector  $\Theta_i$  contains the length-scale parameter  $\alpha_i$  and the variance  $\sigma_i^2$ ,  $i = 1, 2, 3$ . In our implementation we sampled the spectral frequencies associated with  $\alpha_i$  once and adjusted them for each step when optimising  $\alpha_i$ ; see the procedure `PRIOR-FIXED` in Cutajar et al. (2017). The parameters in the variational distribution over  $\mathbf{w}_i$ ,  $i = 1, 2, 3$ , were found using stochastic gradient descent, while expectations taken with respect to  $\mathbf{w}_i$  were approximated using Monte Carlo (similar to what we did in Section 3.5); specifically, we used  $N_{MC} = 25$  Monte Carlo samples.

At each layer we let the number of Fourier features (i.e., sine and cosine basis functions) equal 256 and ran stochastic gradient descent for 50,000 iterations. For the first 10,000

iterations we kept the covariance-function parameters fixed, and optimised the variational parameters for  $w_i, i = 1, 2, 3$ . For the remaining 40,000 iterations we optimised both the weights and covariance-function parameters simultaneously. Each iteration took on the order of a tenth of a second to complete.

### A.3 DGPsparse

The sparse deep Gaussian process model of Damianou and Lawrence (2013) was fitted using the `deepGP` package in `R`, which we provide in the Supplementary Material. We used one hidden layer; specifically, we employed the following hierarchical model,

$$\begin{aligned}\mathbf{Z} \mid \mathbf{Y} &\sim \text{Gau}(\mathbf{Y}, \sigma_\epsilon^2 \mathbf{I}), \\ \mathbf{Y} \mid \mathbf{H}_1 &\sim \text{Gau}(\mathbf{0}, \mathbf{K}_2(\mathbf{H}_1)), \\ \mathbf{H}_1 \mid \mathbf{F}_1 &\sim \text{Gau}(\mathbf{F}_1, \sigma_\xi^2 \mathbf{I}), \\ \mathbf{F}_1 &\sim \text{Gau}(\mathbf{0}, \mathbf{K}_1(\mathbf{S})),\end{aligned}$$

where  $\mathbf{H}_1$  can be seen as jittered versions of the smooth warped locations  $\mathbf{F}_1$ , and  $\mathbf{K}_2$  and  $\mathbf{K}_1$  are given by (A.1) and (A.2), respectively. Sparsity is introduced into the model through the introduction of inducing points and variables for both  $\mathbf{Y}$  and  $\mathbf{F}_1$ . Denote the inducing points for  $\mathbf{F}_1$  as  $\bar{\mathbf{S}}_0$ , and those for  $\mathbf{Y}$  as  $\bar{\mathbf{S}}_1$ , and denote the corresponding inducing variables at these points as  $\bar{\mathbf{F}}_1$  and  $\bar{\mathbf{Y}}$ , respectively. Then, omitting the dependence on the inputs and the inducing points,

$$\begin{aligned}p(\mathbf{Z}, \mathbf{Y}, \mathbf{H}_1, \mathbf{F}_1, \bar{\mathbf{Y}}, \bar{\mathbf{F}}_1) &= p(\mathbf{Z} \mid \mathbf{Y})p(\mathbf{Y} \mid \mathbf{H}_1, \bar{\mathbf{Y}})p(\bar{\mathbf{Y}}) \times \\ &\quad p(\mathbf{H}_1 \mid \mathbf{F}_1)p(\mathbf{F}_1 \mid \bar{\mathbf{F}}_1)p(\bar{\mathbf{F}}_1).\end{aligned}$$

Variational Bayes is used to make inference with the deep sparse GP. Specifically, similar to Section 3.5, the marginal likelihood is lower-bounded, and the variational distribution is constrained to take the form

$$\begin{aligned}q(\mathbf{Y}, \mathbf{H}_1, \mathbf{F}_1, \bar{\mathbf{Y}}, \bar{\mathbf{F}}_1) &= p(\mathbf{Y} \mid \mathbf{H}_1, \bar{\mathbf{Y}})q(\mathbf{H}_1)q(\bar{\mathbf{Y}}) \times \\ &\quad p(\mathbf{F}_1 \mid \bar{\mathbf{F}}_1)q(\bar{\mathbf{F}}_1).\end{aligned}$$

The package `deepGP` implements the approach of Damianou and Lawrence (2013), that is, it finds closed-form expressions for  $q(\bar{\mathbf{F}}_1)$  and  $q(\bar{\mathbf{Y}})$  using free-form optimisation, and constrains  $q(\mathbf{H}_1)$  using a mean-field approach, so that

$$q(\mathbf{H}_1) = \prod_{j=1}^N q(h_{1j}) = \prod_{j=1}^N \text{Gau}(m_{1j}, \sigma_{1j}^2).$$

The  $\{m_{1j}\}$  and  $\{\sigma_{1j}^2\}$  are variational parameters that need to be optimised concurrently with the inducing-point locations  $\bar{\mathbf{S}}_0$  and  $\bar{\mathbf{S}}_1$ , and the model parameters  $\alpha_1, \alpha_2, \sigma_1^2, \sigma_2^2, \sigma_\epsilon^2$ , and  $\sigma_\xi^2$ .

In early attempts to fit the DGPsparse models, we found difficulty optimising the inducing point locations. We hence resorted to fixing these inducing points such that they

are equally spaced in the domain on which they lie, much in the same way as our bijective warpings are rescaled in the SDSP (see (3)). Such a choice rendered the gradient descent optimisation procedure stable and easy to tune. The number of inducing points in each layer can also affect the predictive performance of DGPsparse. In the first case study, we set the number of inducing points in  $\bar{\mathbf{S}}_0$  and  $\bar{\mathbf{S}}_1$  to 10 and 3, respectively. In the second case study, the number of inducing points in  $\bar{\mathbf{S}}_0$  and  $\bar{\mathbf{S}}_1$  were set to 35 and 25, respectively. These numbers reflect those that gave us the best predictive performance after several attempts. We optimised the other parameters concurrently for 5000 iterations, with adaption following the 500th iteration (adaption was carried out by halving the learning rate associated with a parameter every time an associated gradient step decreased the lower-bound, rather than increased it).

After the variational and model parameters were estimated, we computed the predictions and prediction variances of the true process at a set of  $N^*$  prediction locations,  $\mathbf{S}_j^* \equiv (s_j^* : j = 1, \dots, N^*)'$ . Let  $\mathbf{H}_1^* \equiv (h_{1j}^* : j = 1, \dots, N^*)'$  denote the jittered warped inputs at the prediction locations, and  $\mathbf{Y}^* \equiv (Y_j^* : j = 1, \dots, N^*)'$  as the process of interest at these locations. The variational prediction distribution for  $\mathbf{Y}^*$  is given by

$$p(\mathbf{Y}^*|\mathbf{Z}) = \int p(\mathbf{Y}^*|\mathbf{H}_1, \mathbf{H}_1^*, \mathbf{Z})p(\mathbf{H}_1^*|\mathbf{H}_1)q(\mathbf{H}_1)d\mathbf{H}_1^*d\mathbf{H}_1. \quad (\text{A.3})$$

Note that the first term of the integrand of (A.3) is Gaussian, and hence the Monte Carlo approximation

$$p(\mathbf{Y}^*|\mathbf{Z}) \approx \sum_{l=1}^{N_{MC}} p(\mathbf{Y}^*|\mathbf{H}_1^{(l)}, \mathbf{H}_1^{*(l)}, \mathbf{Z}), \quad (\mathbf{H}_1^{(l)}, \mathbf{H}_1^{*(l)}) \sim q(\mathbf{H}_1, \mathbf{H}_1^*),$$

is a Gaussian mixture. Note that  $q(\mathbf{H}_1, \mathbf{H}_1^*) \equiv p(\mathbf{H}_1^*|\mathbf{H}_1)q(\mathbf{H}_1)$  is also Gaussian, and hence easy to sample from. In our implementation we obtained the approximate variational predictive distribution through  $N_{MC} = 100$  Monte Carlo samples.

## A.4 GP

Standard Gaussian process regression was carried out using the Python package `GPflow` (Matthews et al., 2017). We considered zero-mean Gaussian processes with Matérn covariance functions, with smoothness parameters  $\nu = 1/2, 3/2$ , and  $5/2$ . For both case studies best results were obtained with  $\nu = 3/2$ , and hence only results using models with this smoothness parameter are discussed in Section 4.1. In `GPflow`, the length-scale and variance parameters in the Matérn covariance function, as well as the noise variance, are estimated using maximum likelihood, while the prediction and prediction standard errors are obtained using standard Gaussian-process regression equations (e.g., Rasmussen and Williams, 2006, Chapter 2) with the estimated parameters plugged in. Maximum likelihood estimation with GPs with only a few data points is known to be quick. For both case studies optimisation required under a second to complete on our setup.

## A.5 SDSP-MCMC

The SDSP-MCMC model is the same SDSP model used in Section 4.1, but with inference made using MCMC. As in Section A.1, since parameters are difficult to estimate in deep compositional models using MCMC, we fixed the parameters appearing at the top layer and in the observation model to those estimated using variational Bayes. Specifically, the parameters  $\sigma^2$ ,  $l$  (appearing in  $\tau_{n+1}$ ) and  $\sigma_\epsilon^2$  were fixed to 0.442, 0.704 and 0.010132, respectively, in the first case study, and to 0.525, 0.312, and 0.010146, respectively, in the second case study.

MCMC was used to determine the posterior distributions over the weights  $\mathbf{w}_2$  and  $\mathbf{w}_1$  using `Stan` (Carpenter et al., 2017). Ten thousand samples were generated, and the first 1000 were discarded as burn-in, requiring just over an hour of computation time in total. The predictions and prediction standard errors of  $\mathbf{Y}^*$  were then obtained through sampling by composition.

## B Minibatch Stochastic Gradient Descent for Large Datasets

Although all inverses and log-determinants in (5) are relatively small in size and easy to compute, the matrix multiplication  $\mathbf{A}'_{\underline{\Lambda}} \mathbf{A}_{\underline{\Lambda}}$  may become infeasible when the dataset is huge. In such cases, it might be reasonable to instead consider the log-likelihood without  $\mathbf{w}_{n+1}$  integrated out which, due to conditional independence, reduces to a sum over data points, that is,

$$\log p(\mathbf{Z} \mid \mathbf{w}_{n+1}, \underline{\Lambda}, \sigma_\epsilon^2) = \sum_{j=1}^N \log p(Z_j \mid \mathbf{w}_{n+1}, \underline{\Lambda}, \sigma_\epsilon^2), \quad (\text{B.1})$$

where

$$Z_j \mid \mathbf{w}_{n+1}, \underline{\Lambda}, \sigma_\epsilon^2 \sim \text{Gau}(\mathbf{a}_{\underline{\Lambda}}^{(j)'} \mathbf{w}_{n+1}, \sigma_\epsilon^2),$$

and recall that  $\mathbf{a}_{\underline{\Lambda}}^{(j)'}$  denotes the  $j$ th row of  $\mathbf{A}_{\underline{\Lambda}}$ . Now, consider the log-likelihood contribution of a single data point  $Z$ , where  $Z$  is selected uniformly at random from  $\mathbf{Z}$ . Then  $P(Z = Z_j) = 1/N$  for  $j = 1, \dots, N$ , and

$$\begin{aligned} E(\log p(Z \mid \mathbf{w}_{n+1}, \underline{\Lambda}, \sigma_\epsilon^2)) &= \sum_{j=1}^N \log p(Z_j \mid \mathbf{w}_{n+1}, \underline{\Lambda}, \sigma_\epsilon^2) P(Z = Z_j) \\ &= \frac{1}{N} \sum_{j=1}^N \log p(Z_j \mid \mathbf{w}_{n+1}, \underline{\Lambda}, \sigma_\epsilon^2) \\ &= \frac{1}{N} \log p(\mathbf{Z} \mid \mathbf{w}_{n+1}, \underline{\Lambda}, \sigma_\epsilon^2), \end{aligned}$$

from (B.1). Therefore  $N \log p(Z \mid \mathbf{w}_{n+1}, \underline{\Lambda}, \sigma_\epsilon^2)$  is an unbiased estimator of  $\log p(\mathbf{Z} \mid \mathbf{w}_{n+1}, \underline{\Lambda}, \sigma_\epsilon^2)$ , and  $N \nabla \log p(Z \mid \mathbf{w}_{n+1}, \underline{\Lambda}, \sigma_\epsilon^2)$  is an unbiased estimator of  $\nabla \log p(\mathbf{Z} \mid \mathbf{w}_{n+1}, \underline{\Lambda}, \sigma_\epsilon^2)$ .

$\mathbf{w}_{n+1}, \underline{\mathbf{A}}, \sigma_\epsilon^2$ ). Using the unbiased estimate  $N\nabla \log p(Z_j | \mathbf{w}_{n+1}, \underline{\mathbf{A}}, \sigma_\epsilon^2)$  (where  $Z_j$  is randomly sampled from  $\mathbf{Z}$ ) instead of the true gradient based on  $\mathbf{Z}$  when doing gradient descent results in a stochastic gradient descent algorithm.

Similar arguments apply for when grouping the individual data points into minibatches so that

$$\log p(\mathbf{Z} | \mathbf{w}_{n+1}, \underline{\mathbf{A}}, \sigma_\epsilon^2) = \sum_{j=1}^{N_b} \log p(\mathbf{Z}_j^m | \mathbf{w}_{n+1}, \underline{\mathbf{A}}, \sigma_\epsilon^2),$$

where  $N_b$  is the number of minibatches,  $\mathbf{Z}_j^m$  is a minibatch of size  $m_b \ll N$ , and where we have assumed for convenience that  $m_b = N/N_b$  is an integer. In this case

$$\mathbf{Z}_j^m | \mathbf{w}_{n+1}, \underline{\mathbf{A}}, \sigma_\epsilon^2 \sim \text{Gau}(\mathbf{A}_{\underline{\mathbf{A}}}^{(j)} \mathbf{w}_{n+1}, \sigma_\epsilon^2 \mathbf{I}),$$

where  $\mathbf{A}_{\underline{\mathbf{A}}}^{(j)}$  contains the rows of  $\mathbf{A}_{\underline{\mathbf{A}}}$  corresponding to the data in  $\mathbf{Z}_j^m$ . An unbiased estimator of  $\log p(\mathbf{Z} | \mathbf{w}_{n+1}, \underline{\mathbf{A}}, \sigma_\epsilon^2)$  is then given by  $N_b \log p(\mathbf{Z}^m | \mathbf{w}_{n+1}, \underline{\mathbf{A}}, \sigma_\epsilon^2)$  where  $\mathbf{Z}^m$  is a random sample of size  $m_b$  from  $\mathbf{Z}$ .

Minibatches can also be used when modelling the data using an SDSF, except that now  $\mathbf{w}_{n+1}$  and  $\mathbf{F}_{n+1} \equiv \mathbf{Y}$  are not integrated out and instead equipped with a variational distribution  $q(\mathbf{F}_{n+1}, \mathbf{w}_{n+1}) \equiv p(\mathbf{F}_{n+1} | \mathbf{w}_{n+1})q(\mathbf{w}_{n+1})$  where  $p(\mathbf{F}_{n+1} | \mathbf{w}_{n+1})$  is degenerate and  $q(\mathbf{w}_{n+1}) = \text{Gau}(\mathbf{m}_{n+1}, \mathbf{V}_{n+1}(\boldsymbol{\eta}_{n+1}))$ , where  $\mathbf{V}_{n+1}$  is constrained to be diagonal. Omitting details, for this model we have that

$$\mathcal{E}_1 \approx \frac{1}{N_{MC}} \sum_{l=1}^{N_{MC}} \log p(\mathbf{Z} | \mathbf{F}_{n+1}^{(l)}, \sigma_\epsilon^2),$$

where  $\mathbf{F}_{n+1}^{(l)}$  is sampled akin to (12). As shown earlier in this section, it is easy to see that  $N_b \log p(\mathbf{Z}^m | \mathbf{F}_{n+1}^{(l)}, \sigma_\epsilon^2)$  is an unbiased estimator of  $\log p(\mathbf{Z} | \mathbf{F}_{n+1}^{(l)}, \sigma_\epsilon^2)$  and that hence one can write

$$\mathcal{E}_1 \approx \frac{N_b}{N_{MC}} \sum_{l=1}^{N_{MC}} \log p(\mathbf{Z}_j^m | \mathbf{F}_{n+1}^{(l)}, \sigma_\epsilon^2),$$

which can be subsequently used for minibatch stochastic gradient descent.